Impact of Josephson Junction Array modes on Fluxonium Readout

Shraddha Singh,[1, 2, 3, *] Gil Refael,[3, 4] Aashish Clerk,[5, 3] and Emma Rosenfeld[3, †]

[1]*Department of Applied Physics and Physics, Yale University, New Haven, Connecticut 06511, USA*
[2]*Yale Quantum Institute, Yale University, New Haven, Connecticut 06511, USA*
[3]*AWS Center for Quantum Computing, Pasadena, CA 91125, USA*
[4]*Institute for Quantum Information and Matter,*
California Institute of Technology, Pasadena, CA 91125
[5]*Pritzker School of Molecular Engineering, University of Chicago, Chicago, Illinois 60637, USA*
(Dated: December 9, 2024)

Dispersive readout of superconducting qubits is often limited by readout-drive-induced unwanted transitions between qubit levels. While there is a growing understanding of such effects in transmon qubits, the case of highly nonlinear fluxonium qubits is more complex. We theoretically analyze measurement-induced state transitions (MIST) during the dispersive readout of a fluxonium qubit, focusing on a new mechanism: a simultaneous transition/excitation involving the qubit and an internal mode of the Josephson junction array in the fluxonium circuit. Using an adiabatic Floquet approach, we show that these new kinds of MIST processes can be relevant with realistic circuit parameters and relatively low readout drive powers compared to the admissible range of signal-to-noise ratio. As we show, they can also contribute to excess qubit dephasing even after a measurement is complete. We also investigate the dependency of such transitions on the choice of readout frequency and circuit parameters.

I. INTRODUCTION

The fluxonium superconducting qubit, based on a Josephson junction shunted by a capacitor and a large inductance, has emerged as a promising platform for quantum information. It exhibits long lifetimes [1–4], and both single [5] and two-qubit gates [6, 7] have been demonstrated with high fidelity, with potential room for even further improvements [8–12]. The inductive shunt is a crucial part of the fluxonium circuit, with the most common realization being a Josephson junction array (JJA). In regimes where internal array modes are not excited, the JJA can act as a linear superinductance (see e.g. [13, 14]).

The ability to make fast and efficient measurements is equally crucial, in addition to coherence and the ability to do high-fidelity gates, for any qubit platform. Similar to other superconducting qubits, dispersive readout (using a driven readout resonator) has been the standard choice for fluxonium readout (see e.g. [5]). While such measurement schemes should ideally be quantum non-demolition (QND) [15], several experiments have reported non-QND backaction (either enhanced relaxation or transitions to non-computational states) during fluxonium readout [6, 16–18]. Recent theoretical work on driven transmon qubits has provided insights into these so-called measurement-induced state transitions (MIST), showing that multi-photon transitions can lead to resonant excitation of the transmon to higher levels (see e.g. [19–24]).

Similar detrimental transitions need to be examined for fluxonium, to ultimately find means for suppressing such effects. The fluxonium circuit is fundamentally different, and thus, needs independent analysis. For example, the enhanced nonlinearity can dramatically change the number and likelihood of potential
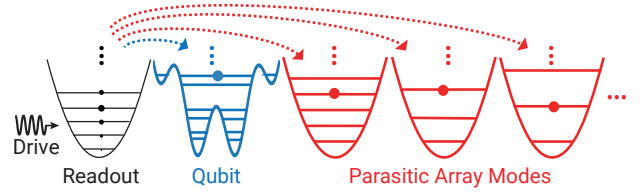
FIG. 1. **Schematic of a PMIST process.** A parasitic effect where energy in a coherent state of the driven readout mode (black) excites extraneous linear modes (red) and the nonlinear qubit mode (blue) simultaneously.

transitions [20, 25]. In this artile, we provide a comprehensive analysis of a unique MIST mechanism in fluxonium that arise due to the internal modes of the JJA during a fluxonium readout (see Fig. 1). We show that for realistic parameters and drive powers, deleterious resonant processes that simultaneously excite the qubit and an internal mode can indeed occur. We term these processes parasitic MIST or PMIST. One can view this as an example of an even more general problem: how is the physics of MIST modified in the presence of a structured environment?

We focus on a heavy fluxonium qubit operated at its flux sweet spot (c.f. Fig. 2), and investigate MIST, keeping the coupling to the most relevant JJA internal modes. We treat the readout as an effective classical drive on the fluxonium-plus-JJA system and use an adiabatic Floquet branch analysis to identify dominant MIST processes. This method was used for transmon studies in Refs. [22, 23]. We also validate this approach through full-time-dependent simulations. Our work goes beyond simply showing that such processes could be relevant. We discuss how they could provide a mechanism for degrading qubit coherence even after measurements are complete (via dephasing from dispersive couplings to the excited internal modes). We also discuss how alternate circuit designs could be employed to help minimize PMIST processes, paying special attention to how modifications

FIG. 2. **Fluxonium readout circuit, qubit and array modes' spectrum.** (a) The color scheme shows primary components that correspond to various modes, shown in Fig. 1 when a JJA fluxonium circuit is connected to a readout resonator (R). The subscripts p, j denote components of the phase-slip junction and the JJA, respectively. This circuit shows coupling capacitances (C_c), readout frequency parameters ($\omega_r = 1/\sqrt{L_R C_R}$), parasitic ground capacitances in JJA ($C_{g,j}$) and next to the phase-slip junction ($C_{g,p}$). The differential capacitance C adjusts the charging energy of the qubit mode (see Table II). (b) Fluxonium mode energy levels in units of h, with the highlighted area showing the first three levels essential for certain readout schemes [5]. (c) Parasitic mode frequencies $\omega_\mu/2\pi$. The lowest even mode $\mu = 2$ has the strongest coupling to the qubit (see Fig. 12).

affect the parasitic mode to qubit coupling strengths. Our analysis here suggests that in optimizing fluxonium readout, parasitic JJA modes introduce additional constraints on the circuit design.

The remainder of this article is structured as follows. Sec. II provides an analysis of the full circuit including fluxonium, JJA, and readout resonator. Using a standard harmonic approximation [26], we derive qubit-parasitic mode couplings strengths, and lower bound parasitic mode effects during readout. Sec. III analyzes readout dynamics, including MIST processes and dephasing from parasitic modes. Sec. IV analyzes the effects of varying coupling strengths between the qubit and a JJA internal mode on PMIST, and investigates different ranges of readout frequencies and parasitic mode frequencies using an energy-conservation picture. In the concluding Sec. V we discuss directions for future work.

N	φ_{ext}	E_{J_p}	E_{C_p}	E_C	E_{C_j}	E_{J_j}	$E_{C_{g,j}}$	$E_{C_{g,p}}$	E_c
122	$0.5\Phi_0$	7.30	1.46	17	0.74	60	194	1.94	19.40

TABLE I. **Circuit parameters for Fig. 2(a) inspired by Ref. [5].** All energies are given in GHz. Here $\Phi_0 = h/2e$ denotes the magnetic flux quantum. The capacitive energies $E_{C'} = \frac{19.4}{C'(\text{fF})}$ GHz are computed from the corresponding capacitances C'. See Table IV in App. B for the values of capacitances.

II. FLUXONIUM READOUT CIRCUIT

We consider a JJA-fluxonium circuit dispersively coupled to a readout mode as shown in Fig. 2. We chose circuit parameters (as listed in Table I) motivated by recent experiments on heavy fluxonium [5–7]. We also restrict attention to the flux "sweet spot" that maximizes qubit coherence. This choice is also expected to reduce the number of allowed transitions in the circuit, as transitions between parity-conserving states via first-order processes are forbidden in this case. For our parameters, the qubit frequency ($\omega_{01}/2\pi$) is ~ 30 MHz and the plasmon frequency (i.e. splitting frequency between first and second qubit excited states $\omega_{12}/2\pi$ is ~ 6 GHz (see Table II for a full list of readout parameters).

Our work specifically investigates the role of the JJA, which comprises the inductive shunt of the fluxonium. The array comprises N junctions and $N-1$ ground capacitances(C_{g_n}) [27]. We neglect disorder effects, and take junction parameters and parasitic ground capacitances to be uniform in the array (i.e. $C_{g_1} = .. = C_{g_N}$). This capacitance value is given by $C_{g,j}$ where the subscript j indicates the parasitic ground capacitance in the JJA [28]. As shown in Fig. 2(a), two additional identical ground capacitances C_{g_0}, C_{g_N} near the phase-slip junctions in blue (see Figs. 2) may have different values compared to those in the interior of the array, i.e. $C_{g_0} = C_{g_N} \equiv C_{g,p} \neq C_{g,j}$. Note that the subscript p indicates the parasitic ground capacitances next to the phase-slip junction.

The JJA fluxonium circuit has N internal degrees of freedom [26, 29]: one qubit mode (ϕ) and $N-1$ internal modes ($\mu = 1, 2, ..., N-1$). These internal modes are coupled via the ground capacitances and are referred to as the "parasitic" modes of the JJA. In our notation, we label the readout mode as r. The charge and flux quadratures of the qubit mode are denoted by $\hat{N}_\phi$ and $\hat{\phi}$ where $[\hat{\phi}, \hat{N}_\phi] = i\hbar$. We simplify the problem by treating all but the qubit mode as harmonic oscillators [23, 26, 29]. We denote the photon loss and gain operators of the linear modes r, μ using $\hat{a}_r, \hat{a}_\mu$ and $\hat{a}_r^\dagger, \hat{a}_\mu^\dagger$, respectively. This assumption presents the best-case scenario for JJA-fluxonium readout. In practice, the JJA nonlinearity could increase the PMIST but the numerical analysis of such a system would quickly become intractable. We expect that our analysis shows the least number of detrimental effects of the JJA parasitic modes on the qubit performance of a driven fluxonium circuit.

Setting $\hbar = 1$, the Hamiltonian of our fluxonium circuit has the form (see App. A for derivation)

$$\hat{H} = \hat{H}_\phi + \hat{H}_\mu + \hat{H}_r + \hat{H}_{\text{int}}, \tag{1}$$

where the qubit Hamiltonian $\hat{H}_\phi$ (with JJA inductive energy $E_L = E_{J_j}/N$) is

$$\hat{H}_\phi/2\pi = 4\tilde{E}_c^\phi \hat{N}_\phi^2 + E_{J_p} \cos\hat{\phi} + E_L \hat{\phi}^2/2, \tag{2}$$

the junction array and readout Hamiltonians are $\hat{H}_\mu = \sum_\mu \omega_\mu \hat{a}_\mu^\dagger \hat{a}_\mu$ and $\hat{H}_r = \omega_r \hat{a}_r^\dagger \hat{a}_r$, respectively. The

Qubit (ϕ) &	$\omega_{01}/2\pi$	$\omega_{12}/2\pi$	$\tilde{E}_c^\phi$	$g_{\phi r}/2\pi$	$\chi_{\phi r}(01)/2\pi$	$\chi_{\phi r}(12)/2\pi$	$\omega_{\rm r}/2\pi$	$\kappa_{\rm r}/2\pi$
Readout (r)	30 MHz	6.04 GHz	0.92 GHz	25.50 MHz	0.18 MHz	0.98 MHz	8.50 GHz	1 MHz
Parasitic-Mode				$g_{\phi\mu}/2\pi$	$g_{\mu r}/2\pi$	$\chi_{\phi\mu}(01)/2\pi$	$\chi_{\phi\mu}(12)/2\pi$	$\omega_\mu/2\pi$	Q_μ
($\mu = 2$)				157 MHz	4.22 MHz	-1.10 MHz	5 MHz	12.06 GHz	10^4

TABLE II. **Measurement parameters for qubit mode ϕ, readout mode r and closest even parasitic mode $\mu = 2$.** All quantities are derived and computed analytically using circuit parameters listed in Table I (see Apps. A-B for details). **Qubit-Readout Parameters:** (ω_{ij}) qubit $i \to j$ splitting frequency between fluxonium excited states i, j; ($\tilde{E}_c^\phi$) qubit charging energy; ($g_{\phi r}$) qubit-readout coupling; ($\chi_{\phi r}(ij)$) dispersive shift due to readout mode in the two-level ij system; ($\omega_{\rm r}$) readout mode frequency; ($\kappa_{\rm r}$) decay rate of the readout resonator. **Parasitic-Mode Parameters:** ($g_{\phi\mu}$) qubit-parasitic coupling; ($g_{\mu r}$) parasitic-readout coupling; ($\chi_{\phi\mu}(ij)$) dispersive shift due to parasitic mode μ in the two-level ij system; (ω_μ) mode frequency; and (Q_μ) internal quality factor inspired by [13].

qubit charging energy $\tilde{E}_c^\phi$ (see Table II) deviates from the target value of $E_c^\phi = 1$ GHz due to parasitic capacitance. The coupling between the three modes is described by the interaction Hamiltonian

$$\hat{H}_{\rm int} = \sum_\mu g_{\phi\mu} \frac{\hat{N}_\phi}{N_{\phi,\rm ZPF}} (\hat{a}_\mu - \hat{a}_\mu^\dagger)$$
$$- g_{\phi r} \frac{\hat{N}_\phi}{N_{\phi,\rm ZPF}} (\hat{a}_{\rm r} - \hat{a}_{\rm r}^\dagger)$$
$$- \sum_\mu g_{\mu r} (\hat{a}_{\rm r} - \hat{a}_{\rm r}^\dagger)(\hat{a}_\mu - \hat{a}_\mu^\dagger). \tag{3}$$

where for our parameters, the zero-point fluctuations of qubit charge $N_{\phi,\rm ZPF} = 0.36$. Values for all remaining parameters appearing here are given in Table II. Explicit expression for the $g_{\phi\mu}$ are discussed in Sec. IV, while expressions for all other variables can be found in App. B.

We verify the conclusion from Ref. [26] that the symmetry of the parallel circuit in Fig. 2(a) prevents coupling between odd parasitic modes (including $\mu = 1$) and other circuit modes. We extend this result to two additional circuits, with different ground circuit configurations, showing qualitatively consistent conclusions across all three circuits in App. A. The circuits yield the same Hamiltonian when the differential capacitance C and coupling capacitance C_c are altered such that qubit frequency and qubit-readout coupling are the same across all three circuits (see Table V in App. A).

We find that the lowest-frequency even parasitic mode $\mu = 2$ has the strongest coupling to the qubit mode (see Fig. 12 in App. B 1); corresponding parameters are listed in Table II. Moreover, Fig. 12 shows that the $\mu = 2, 4, 6$ parasitic modes couple to the qubit with a strength $g_{\phi\mu}$ that is stronger than the qubit-readout coupling $g_{\phi r}$. This relative behavior between coupling strengths has also been pointed out previously in Ref. [26].

Given these insights, in the rest of this work we will focus on the parallel circuit from Fig. 2 using parameters given by Tables I-II in Eq. 1. Further, our description will only retain the strongest coupled parasitic mode $\mu = 2$, along with the qubit and readout resonator. For details on other parasitic modes and their parameters, see App. B 1. Note that for our chosen parameters (see Table I), the qubit couples roughly six times more strongly to the parasitic mode at $\mu = 2$

than it does to the readout r [30]. We will show that this strong coupling implies that the parasitic mode can play a strong role in measurement-induced state transitions, i.e. the PMIST effect that is the subject of this work.

III. PARASITIC-MODE-INDUCED STATE TRANSITIONS: PMIST

In this section, we analyze how the presence of a parasitic mode ($\mu = 2$) affects the dynamics of a driven fluxonium circuit during a readout pulse. To simulate the linear drive on the readout resonator, we add a drive term $\hat{V}_{\rm d} = i\xi(\hat{a}_{\rm r} - \hat{a}_{\rm r}^\dagger) \cos \omega_{\rm d} t$ to the system Hamiltonian in Eq. 1. If we consider the fluxonium qubit mode, parasitic modes, and readout resonator, a full numerical analysis of several excitations in the circuit would require a prohibitively large Hilbert space. To truncate our Hilbert space to feasible dimensions for numerical simulations, here we only include a single parasitic mode $\mu = 2$ (as previously justified in Sec. II), and we replace the readout mode with a classical drive term [20, 22, 23] (see derivation in App. C 1). Under this semi-classical approximation, the driven circuit Hamiltonian includes the qubit mode ϕ and the parasitic mode at $\mu = 2$, and is

$$\hat{H}_{s.c.}(\bar{n}_{\rm r}) = \hat{H}_0 + \hat{V}_{s.c.}(\bar{n}_{\rm r}). \tag{4}$$

Here, the bare Hamiltonian is

$$H_0 = \hat{H}_\phi + \hat{H}_\mu - \frac{g_{\phi\mu}}{N_{\phi,\rm ZPF}} \hat{N}_\phi (\hat{a}_\mu - \hat{a}_\mu^\dagger) \tag{5}$$

and the modified drive term $V_{s.c.}$ is

$$\hat{V}_{s.c.}(\bar{n}_{\rm r}) = \frac{\xi_{\phi r}(\bar{n}_{\rm r})}{N_{\phi,\rm ZPF}} \hat{N}_\phi \cos \omega_{\rm d} t + \frac{\xi_{\mu r}}{N_{\mu,\rm ZPF}} (\bar{n}_{\rm r}) \hat{N}_\mu \cos \omega_{\rm d} t, \tag{6}$$

where the effective drive amplitudes $\xi_{\mu(\phi)r}(\bar{n}_{\rm r}) = 2g_{\mu(\phi)r}\sqrt{\bar{n}_{\rm r}}$, and $\bar{n}_{\rm r}$ denotes the average number of photons in the readout cavity. In the remaining text, we refer to the quantities $\xi_{\phi r/\mu r}$ as "qubit drive strengths" and "parasitic drive strengths", respectively.

Our primary focus is to analyze PMIST processes that introduce simultaneous transitions in the parasitic mode and the qubit mode. To identify the likely

state transitions in the driven circuit, we first examine the energy eigenstates of the bare Hamiltonian $\hat{H}_0$ in Eq. 5. These states will be hybridized fluxonium-parasitic mode states, and we label them as $|\tilde{k}, \tilde{n}\rangle$. A given state $|\tilde{k}, \tilde{n}\rangle$ corresponds to the eigenstate that has the maximum overlap with "bare" fluxonium and parasitic mode states $|k\rangle_\phi \otimes |n\rangle_\mu$, i.e., the eigenstates of H_ϕ and H_μ.

In what follows, we identify relevant state transitions in the driven fluxonium plus parasitic mode system. First, we perform an analysis based on the Floquet eigenstates of our system at a given fixed drive power [21–23]. We can use this to then simulate the drive ring-up to some chosen final photon number $\bar{n}_r$, and identify potential state transitions. We do this for a range of drive frequencies ω_d. We find that the presence of the parasitic mode $\mu = 2$ significantly increases the number of MIST processes in the system. We analyze the processes that cause these transitions and quantify their rates using perturbative approaches and Landau Zener probability calculations [31]. We also show that the residual population in the parasitic modes, after a readout pulse, can lead to significant dephasing of the reset qubit mode, limiting the performance of the qubit for future use.
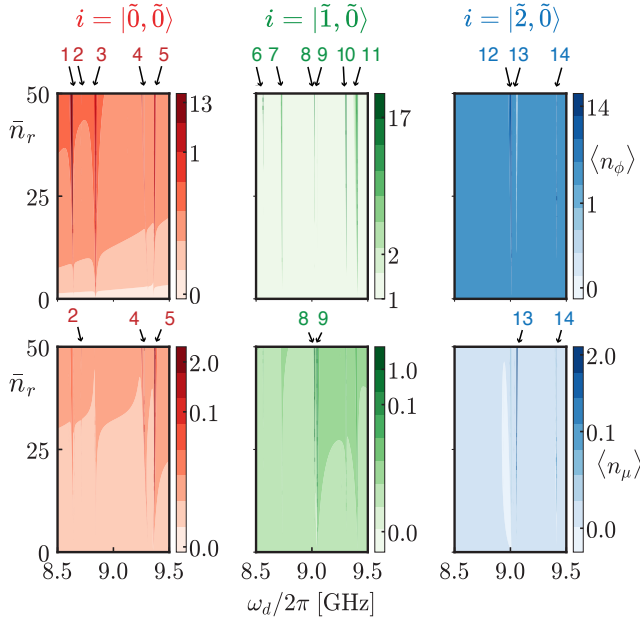
A. Floquet branch analysis method

FIG. 3. **MIST and PMIST processes as seen in Floquet branch simulations.** Each column corresponds to the branch associated with a specific undriven (but dressed) eigenstate $i = |\tilde{k}, \tilde{0}\rangle$. **Top row:** Average fluxonium excitation number in the given branch $\langle n_\phi \rangle$, as a function of drive power ($\propto \bar{n}_r$) and drive frequency ω_d. **Bottom row:** Average excitation number of the $\mu = 2$ parasitic mode, $\langle n_\mu \rangle$. Color scales use a log scaling to help visualize all transitions. Arrows and numbers are used to indicate each transition (with numbers corresponding to Table III). See Figs. 20-22 of App. C 3 b for corresponding behaviour of quasienergies.

Our first numerical analysis involves calculating the Floquet eigenstates of $H_{s.c.}$ (see Eq. 4) for various fixed values of the drive powers, as controlled by the average photon number $\bar{n}_r$. We do this by retaining the lowest 20 levels in the qubit subspace ϕ and 2 levels in the parasitic mode $\mu = 2$[32]; the truncation for this analysis are discussed further in App. C 2. Our goal is to use these results to make predictions for a readout pulse involving a time-dependent drive power, identifying possible transitions starting from a dressed state $|i\rangle = |\tilde{\phi}, \tilde{\mu}\rangle$ where $\phi \in \{0, 1, 2\}$ and $\mu = 0$ (i.e. parasitic mode is initially empty). With $\omega_\mu/2\pi = 12.06$ GHz, the analysis in this section will consider the regime of negative detuning where, $\omega_{\mu=2} > \omega_d = \omega_r \gg \omega_q$, and can be replicated for any other parasitic mode $\mu \neq 2$. Note that we also analyze the effects of an alternative circuit with $\omega_{\mu=2}/2\pi \sim 16$ GHz and $\omega_{01}/2\pi \sim 300$ MHz in Sec. IV.

Inspired by [22, 23], we extract PMIST processes by tracking the evolution of the Floquet eigenstates as we increase the parameter $\bar{n}_r$, a method known as *branch analysis*. We do this for a series of discrete values of $\bar{n}_r$, that we chose to be integers. The simulation begins in a chosen eigenstate $|i\rangle_0$ of the bare Hamiltonian $\hat{H}_0 \equiv \hat{H}_{s.c.}[\bar{n} = 0]$ (see Eq. 5). Next, we compute the Floquet eigenstates $|m_1\rangle$ of the Hamiltonian $\hat{H}_{s.c.}[\bar{n}_r = 1]$, corresponding to a single photon increase in the readout resonator. We then identify the Floquet eigenstate of this Hamiltonian $|i\rangle_{\bar{n}_r=1}$ that has maximum overlap with $|i\rangle_{\bar{n}_r=0}$. We repeat this process iteratively, increasing $\bar{n}_r$ by one each time:

$$|i_{\bar{n}_r=l}\rangle : \max_m |\langle i_{\bar{n}_r=l-1}|m_{\bar{n}_r=l}\rangle|^2. \tag{7}$$

We thus obtain a set of states $|i\rangle_0, |i\rangle_1, |i\rangle_2, ...$ that we refer to as a branch. At a heuristic level, this trajectory of states would describe the adiabatic evolution of the system as the drive power is increased. The drive power in this trajectory is increased to emulate a single photon increase in the readout resonator i.e. $\delta\bar{n}_r = 1$. This corresponds to a constant increase in drive powers (see Eq. 6) $\delta|\xi_{\mu(\phi),r}|^2 = 4g_{\mu(\phi),r}^2$. We make this choice to emulate the more quantum approach to a branch analysis captured in Ref. [19, 23]. The probability for this ring up is studied further for one of the transitions in Sec. III C. We emphasize that our analysis shows the impact of PMIST transitions and does not focus on identifying *all* transitions that will be caused due to the N parasitic modes in the fluxonium circuit.

We make these choices to observe population change in the fluxonium potential, i.e. state transitions, as we ring up the drive powers. In Eq. 7, the overlaps between Floquet eigenstates are all computed at a fixed time within each drive period (i.e. at times $t_l = 2\pi l/\omega_d$). We have verified that our method yields the same results as Ref. [23] (where instead a time-averaged overlap was used). Note that, the slower or more adiabatic the ring-up of the drive, more are the chances to observe a state transition. To avoid fairly weak transitions we ring-up the drive using discrete steps of $\delta\bar{n}_r = 1$ which corresponds to a linear increase in the drive powers. This choice uses a drive

Transition No. (see Fig. 3)	Fluxonium MIST Process	Threshold Drive Photon ($\bar{n}_r$)	Drive Frequency ($\omega_d/2\pi$)	Quasienergy Gap (Δ_{ac})	PMIST	Drive Photons Absorbed (see Fig. 8)
1.	$|\tilde{0},\tilde{0}\rangle \longleftrightarrow |\tilde{13},\tilde{0}\rangle$	13	8.64 GHz	0.90 MHz	×	3
2.	$|\tilde{0},\tilde{0}\rangle \longleftrightarrow |\tilde{4},\tilde{2}\rangle^*$	48	8.71 GHz	0.06 MHz	✓	4
3.	$|\tilde{0},\tilde{0}\rangle \longleftrightarrow |\tilde{8},\tilde{0}\rangle$	~ 0	8.84 GHz	−	×	2
4.	$|\tilde{0},\tilde{0}\rangle \longleftrightarrow |\tilde{6},\tilde{1}\rangle^*$	46	9.25 GHz	1.63 MHz	✓	2
5.	$|\tilde{0},\tilde{0}\rangle \longleftrightarrow |\tilde{3},\tilde{1}\rangle$	12	9.36 GHz	0.56 MHz	✓	2
6.	$|\tilde{1},\tilde{0}\rangle \longleftrightarrow |\tilde{17},\tilde{0}\rangle$	32	8.56 GHz	0.25 MHz	×	4
7.	$|\tilde{1},\tilde{0}\rangle \longleftrightarrow |\tilde{7},\tilde{0}\rangle$	4	8.73 GHz	0.74 MHz	×	2
8.	$|\tilde{1},\tilde{0}\rangle \longleftrightarrow |\tilde{12},\tilde{1}\rangle$	19	9.02 GHz	0.12 MHz	✓	4
9.	$|\tilde{1},\tilde{0}\rangle \longleftrightarrow |\tilde{2},\tilde{1}\rangle$	11	9.05 GHz	0.66 MHz	✓	2
10.	$|\tilde{1},\tilde{0}\rangle \longleftrightarrow |\tilde{14},\tilde{0}\rangle$	7	9.31 GHz	0.50 MHz	×	3
11.	$|\tilde{1},\tilde{0}\rangle \longleftrightarrow |\tilde{9},\tilde{0}\rangle$	2	9.41 GHz	1.19 MHz	×	2
12.	$|\tilde{2},\tilde{0}\rangle \longleftrightarrow |\tilde{12},\tilde{0}\rangle$	3	9.00 GHz	0.73 MHz	×	2
13.	$|\tilde{2},\tilde{0}\rangle \longleftrightarrow |\tilde{0},\tilde{2}\rangle$	38	9.06 GHz	0.53 MHz	✓	2
14.	$|\tilde{2},\tilde{0}\rangle \longleftrightarrow |\tilde{5},\tilde{1}\rangle^*$	49	9.41 GHz	2.71 MHz	✓	2

TABLE III. **Measurement-induced-state-transition (MIST) observed in Fig. 3.** Column 1 lists the numbering used to mark the transitions in Fig. 3. Here $|\tilde{i},\tilde{j}\rangle$ indicates the hybridized eigenstate of H_0 (see Eq. 5) which has the maximum overlap with the state $|i\rangle_\phi \otimes |j\rangle_{\mu=2}$ in the disjoint Hilbert space of qubit mode (ϕ) and parasitic mode ($\mu = 2$). Column 2 lists the MIST processes that start at the lowest average readout photon number $\bar{n}_r$ given by column 3. In some cases, we use $\bar{n}_r \sim 0$ to indicate that the drive frequency is exactly resonant with the transition frequency between the two levels. A '*'-marked state indicates hybridization at lower $\bar{n}_r$ due to preceding transitions [a]. Column 4 represents the drive frequency $\omega_d/2\pi$ at which these transitions occur. Column 5 yields the quasienergy gap at the avoided crossing labeled as Δ_{ac}. Column 6 indicates if the process cannot occur without the parasitic mode, denoted as PMIST. The various colors for the checkmarks indicate that the PMIST event involves the state $|\tilde{0},\tilde{0}\rangle$ (red), $|\tilde{1},\tilde{0}\rangle$ (green) or $|\tilde{2},\tilde{0}\rangle$ (blue). Column 7 indicates the number of drive photons (#) involved in the energy-conserving process, illustrated in Fig. 8, which is responsible for these transitions.

[a] $|\tilde{4},\tilde{2}\rangle^*$: $|\tilde{4},\tilde{2}\rangle \longleftrightarrow |\tilde{14},\tilde{2}\rangle$ at $\bar{n}_r = 5, \omega_d/2\pi = 8.71$ GHz with $\Delta_{ac} = 4.0$ MHz absorbs 2 drive photons
$|\tilde{6},\tilde{1}\rangle^*$: $|\tilde{6},\tilde{1}\rangle \longleftrightarrow |\tilde{3},\tilde{1}\rangle$ at $\bar{n}_r \sim 0, \omega_d/2\pi = 9.25$ GHz
$|\tilde{5},\tilde{1}\rangle^*$: $|\tilde{5},\tilde{1}\rangle \longleftrightarrow |\tilde{17},\tilde{0}\rangle$ at $\bar{n}_r = 14, \omega_d/2\pi = 9.41$ GHz with $\Delta_{ac} = 4.2$ MHz absorbs 1 drive photon

strength increment size $\delta|\xi_{\phi(\mu),r}| = 2g_{\phi(\mu),r}$, different from the driven transmon analysis in Refs. [23] where $\delta|\xi_{\phi,r}| \sim \kappa_r$, the readout resonator's decay rate. Thus, our simulations can also be used to understand the impact of parasitic state transitions due to a linearly increasing drive on the fluxonium circuit.

For each state $|i_{\bar{n}_r=k}\rangle$ in a given branch, we compute:

1. The expectation value of the fluxonium excitation-number operator $\hat{n}_\phi = \sum_k k |k\rangle_\phi \langle k|_\phi$, where $|k\rangle_\phi$ is the kth bare fluxonium energy eigenstate,

2. The expectation value of parasitic-mode number operator $\hat{n}_\mu = \hat{a}_\mu^\dagger \hat{a}_\mu$ (for the single mode $\mu = 2$ that we retain), and

3. The quasi-energy of the state E_i mod ($\omega_d/2\pi$).

We can thus identify MIST and PMIST transitions by detecting sudden changes in the number of qubit or parasitic mode excitations as the $\bar{n}_r$ is increased, indicating an unwanted drive-induced hybridization of eigenstates.

B. Branch analysis PMIST predictions

Fig. 3 illustrates our main result, showing examples of PMIST drive-induced transitions, for initial states that have maximum overlap with states $|0\rangle_\phi$, $|1\rangle_\phi$ and $|2\rangle_\phi$ in the fluxonium subspace and the ground state $|0\rangle_{\mu=2}$ in the parasitic subspace. For each branch, we use color map to plot the average excitation number of the qubit mode $\langle n_\phi \rangle$ (top row), and the parasitic mode $\langle n_\mu \rangle$, range of readout drive frequencies (horizontal axes) and final readout cavity average photon numbers $\bar{n}_r$ (vertical axes).

Note that both the drive powers, of the qubit $\xi_{\phi r}$ and of the parasitic mode $\xi_{\mu r}$, are exclusively dependent on $\bar{n}_r$. Thus, we will often interchangeably call $\bar{n}_r$ as the drive power. Results are shown for driven frequencies $\omega_d/2\pi$ in the range $8.5 - 9.5$ GHz [33]; other regimes are discussed in Sec. IV. For one-dimensional slices of the results at fixed $\bar{n}_r$, along with the quasi-energies, see App. C 3 b.

Any streak or sharp change in color intensity represents a sudden and significant jump in the qubit or parasitic mode population, i.e. MIST or PMIST. The parasitic transitions or PMIST correspond to si-

multaneous jumps in the population of the modes ϕ (Figs. 3, top row) and $\mu = 2$ (Figs. 3, bottom row), as $\bar{n}_r$ varies. At these points, an avoided crossing in the quasi-energies of the Floquet states confirms the hybridization of the two states involved in the population exchange (see Figs. 20-22 in App. C 3 b). Additional resonances may occur at alternate drive frequencies not shown in Fig. 3. Table III lists significant transitions observed in our Floquet simulations, and associated processes which cause them, identified through a perturbative analysis (see App. C 3 b) and energy conservation (shown later in Fig. 8). We note that certain MIST processes, including PMIST, involve transitions at the flux sweet spot [34] between parity-conserving states, due to virtual excitations via non-parity-conserving states.

The above results clearly show that coupling to the JJA parasitic modes enables new MIST processes (beyond what would be predicted by a fluxonium-only simulation). Further, we find that coupling to parasitic modes can alter and even disrupt transitions that would be predicted by a fluxonium-only calculation. For example, consider transition 14 in Table III. For this drive frequency, if one neglects the qubit-parasitic mode coupling, one finds a MIST transition between $|\tilde{2}, \tilde{0}\rangle \leftrightarrow |\widetilde{17}, \tilde{0}\rangle$ will occur via the absorption of three drive photons. Including the parasitic mode, the nature of this process changes. As drive power (i.e. $\bar{n}_r$) is increased, one first finds a transition between the states $|\tilde{5}, \tilde{1}\rangle \leftrightarrow |\widetilde{17}, \tilde{0}\rangle$ at a threshold drive photon of $\bar{n}_r = 14$. As the drive power is further increased, one obtains at $\bar{n}_r = 41$ a transition $|\tilde{2}, \tilde{0}\rangle \leftrightarrow |\tilde{5}, \tilde{1}\rangle$ (something enabled by the earlier hybridization of $|\tilde{5}, \tilde{1}\rangle$ and $|\widetilde{17}, \tilde{0}\rangle$).

Another qualitatively new feature that arises due to the parasitic modes is the possibility of MIST-like transitions where the qubit loses excitations. For example, consider transition 12 in Table III. In this process, two drive photons are absorbed, the fluxonium state has a downward transition $|2\rangle_\phi \rightarrow |0\rangle_\phi$, and the net energy released is used to excite the parasitic mode $|0\rangle_\mu \rightarrow |2\rangle_\mu$ By simple energy conservation, such an effect is not possible without a parasitic mode. In fact, this transition can even modify the T_1 lifetime of the $0 - 2$ fluxonium subspace, and not just contribute to leakage like general MIST phenomena.

Our results also display branch bunchings (see Figs. 20, sub-panels (2) and (4), in App. C 3 b for reference) instead of crossings in the negative detuning regime. This is contrary to Ref. [23] where such branch bunching has been observed only in the positive detuning ($\omega_q > \omega_r$) regime. Consider for example transitions 3 and 4 in Table III. Here, we are driving at a frequency that exactly matches the transition frequency between two non-computational states, such that these states immediately start to hybridize into an equal superposition of the two original undriven states. For example, in transition 4, the readout drive frequency exactly matches the $|3\rangle_\phi \rightarrow |6\rangle_\phi$ transition frequency at zero readout excitations. In this case, levels $|3\rangle_\phi$ and $|6\rangle_\phi$ hybridize for any non-zero drive power $\bar{n}_r$ (see Fig. 20 in App. C 3 b). While this effect is not limited to PMIST, we highlight that the pres-
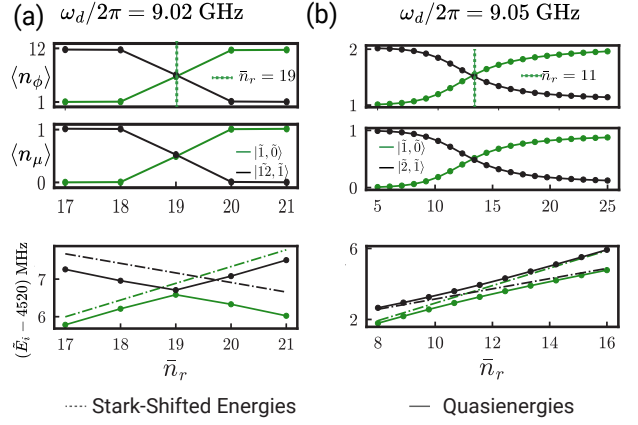

FIG. 4. **PMIST processes including state $|\tilde{1}, \tilde{0}\rangle$.** Examples of PMIST using transitions **(a)** 8 and **(b)** 9 from Table III involving the $|\tilde{1}, \tilde{0}\rangle$ state, with maximum overlap to the un-hybridized state $|1\rangle_\phi \otimes |0\rangle_{\mu=2}$. **Top row:** Qubit mode average occupation $\langle n_\phi \rangle$. **Middle row:** Parasitic mode average occupation $\langle n_\mu \rangle$. **Bottom row:** $\tilde{E}_i = E_i \bmod \omega_d$ where E_i is the Stark-shifted eigen-energy (dashed) obtained from first-order perturbative calculations, or quasi-energy (solid) obtained from Floquet simulations showing avoided crossings. Plots are extracted from numerical data used in Fig. 3. The data points are connected by lines for visual aid.

ence of parasitic modes can result into more exotic transitions transitions. For example, in transition 4, one such transition between the states $|\tilde{3}, \tilde{1}\rangle$ and $|\tilde{6}, \tilde{1}\rangle$, where the parasitic mode was excited, eventually lead to a PMIST effect involving the computational state $|\tilde{0}, \tilde{0}\rangle$. See Fig. 20, sub-panel (4), for explicit population and quasienergy plots involving the three states.

Our findings reveal that for our specific circuit choice, JJA parasitic modes can become significantly populated, as we show in Fig. 3. Having identified key transitions that cause these effects, we now calculate the transition rates in detail, and the consequence on qubit coherence.

For further insights, we now examine in more detail how the quasienergies and excitation numbers change as a function of drive power $\bar{n}_r$ when we pass through an avoided crossing associated with a PMIST process. Figs. 4(a,b) show explicitly how average qubit and parasitic mode excitation numbers change as a function of drive powers $f(\bar{n}_r)$ for fixed drive frequency corresponding to 8, 9 (respectively) in Table III. Both these transitions involve starting in the qubit's first excited state (i.e. branches associated with the undriven state $|\tilde{1}, \tilde{0}\rangle$). The simultaneous exchange of population in the qubit mode ϕ, shown in the top panels, and the parasitic mode $\mu = 2$, shown in the middle panels, confirms that the transitions are indeed PMIST.

The bottom panel of Fig. 4 shows the corresponding behavior of the branch quasi-energies as a function of drive power, for the same drive parameters. We both plot quasi-energies coming from the Floquet calculations, as well as the predictions of a perturbative calculation including drive-induced Stark shifts (see App. C 3 a for details). For Fig. 4, the perturbative
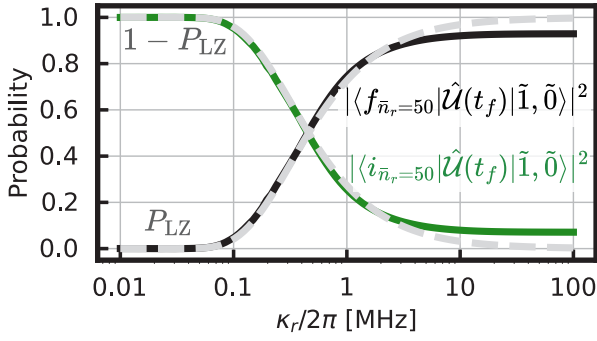
FIG. 5. **PMIST transition probabilities as a function of readout cavity ring-up rate.** We plot the probabilities for adiabatic (green) and diabatic (black) transitions for a time-dependent ring-up of the average cavity photon number from $\bar{n}_r = 0$ to $\bar{n}_r = 50$, for different choices of the cavity damping rate κ_r which controls the speed of the sweep (see text). We start the system in the qubit's first excited state $|\tilde{1}, \tilde{0}\rangle$. The drive frequency is $\omega_d/2\pi = 9.05$ GHz, corresponding to the crossing shown in in Fig. 4(b). Here, $|f_{\bar{n}_r=50}\rangle$ and $|i_{\bar{n}_r=50}\rangle$ are the final states in the end of branch analyses for $|\tilde{2}, \tilde{1}\rangle$ and $|\tilde{1}, \tilde{0}\rangle$, respectively. The time-evolution operator is denoted by $\hat{\mathcal{U}}(t_f) = \mathcal{T}\exp\left(-i\int_0^{t_f}\hat{H}_{s.c.}(t)dt\right)$ where $\mathcal{T}$ indicates time-ordering and $t_f = 10/\kappa_r$. The adiabatic (green) curve corresponds to an unwanted PMIST transition. We also plot the predictions of the Floquet branch analysis combined with a Landau Zener approximation for the probabilities (gray), which are in excellent agreement over a wide range of κ_r.

calculations predict the onset of an avoided-crossing at a drive power close to the value derived from the Floquet simulations. Note that these transitions occur at relatively modest average readout cavity photon numbers $\bar{n}_r = 11, 19$.

C. Transition probability

Our Floquet branch analysis gives strong evidence that MIST and PMIST transitions will occur during the ring-up of the resonant during a readout pulse. Here, we validate this approach by focusing on a specific transition, and we show (via explicit time-dependent simulations) that it occurs as predicted. We also show that this full-time-domain simulation is in agreement with a Landau-Zener analysis that takes as inputs the result of the Floquet branch analysis.

We focus on the PMIST transition shown in Fig. 4(b), which corresponds to an avoided crossing energy gap of $\Delta_{ac} = 0.66$ MHz. We will perform a full time-dependent simulation of $\hat{H}_{s.c.}$ in Eq. 4, using time-dependent drive powers that are determined by a time-dependent average readout cavity photon number having the form:

$$\bar{n}_r(t) : \bar{n}_r(1 - e^{-\kappa_r t/2})^2. \tag{8}$$

This corresponds to the ring-up of a resonantly driven cavity with a damping rate κ_r [21–23].

To calculate transition probabilities in this full-time-dependent simulation, we initiate the system in

the dressed state $|\tilde{1}, \tilde{0}\rangle$, evolve under $\hat{H}_{s.c.}(t)$ from a time $t = 0$ to $t = 10/\kappa_r$, and then compute the overlap of this state with the Floquet branches of the two states $|i\rangle = |\tilde{1}, \tilde{0}\rangle$ and $|f\rangle = |\tilde{2}, \tilde{1}\rangle$ associated with our predicted transition. We then repeat this calculation for different choices of κ_r, examining how the transition probabilities vary, with the results shown in Fig. 5. As expected, the probability of remaining adiabatic (green curve) decreases as one increases κ_r. Note here that at large κ_r, adiabatic evolution corresponds to a detrimental PMIST transition having occurred as the most likely final state $|\tilde{2}, \tilde{1}\rangle$ has an extra qubit and parasitic mode excitation compared to the initial state $|\tilde{1}, \tilde{0}\rangle$.

For small κ, the above probabilities are in agreement with the predictions of our Floquet branch analysis combined with a Landau-Zener approximation to the probability of a non-adiabatic transition [23, 31] (see App. C 3 c). These probabilities (P_{LZ}) are shown in gray in Fig. 5. We see agreement for most of the values of κ_r between the time-domain simulations and our Landau-Zener calculations using the Floquet quasi-energies. [SS: However, for large $\kappa_r \to \infty$, we observe a small disagreement indicating a hybridization of the two levels involved in the transition. The sum of probabilities of being in the two states is always 1, and so, this does not indicate a transition effect which involves a third level either. We attribute this deviation to the complexity of our two-mode system which is very likely to not be explained by the simple picture presented by the Landau Zener physics of a two-level system.]

D. Post-readout qubit dephasing

The new PMIST processes we identify here can also potentially create errors *after* the readout pulse is complete, as they lead to a new dephasing channel. A PMIST process results in a JJA parasitic mode having a residual excitation post readout. As there is a non-zero dispersive coupling $\chi_{\mu\phi}$ between these modes and the qubit, and as these modes are believed to have relatively large internal quality factors $Q \sim 10^4$ [13, 35], this will lead to the qubit acquiring a random phase (tied to the random time at which the parasitic mode relaxes). Below, we show master equation simulation results which quantify the scale of phase errors that would result from such processes.

For concreteness, we consider a readout pulse with a frequency corresponding to the PMIST transition labeled 9 in Fig. 4(b)), and for a cavity damping rate $\kappa_r/2\pi = 1$ MHz (which determines the ring-up time of the cavity to the maximum drive powers given by $\bar{n}_r = 50$). For these parameters, our previous simulations and Landau-Zener analysis suggest that at the end of the readout pulse, the parasitic mode will have an average non-zero excitation $\langle n_\mu \rangle = 0.25$. In fact, for many transitions this population can be as high as $\langle n_\mu \rangle = 2.0$ as shown in Table III. We now ask how the decay of such population will dephase the fluxonium (assuming it is prepared after readout in the state $|+\rangle = \frac{|0\rangle_\phi + |1\rangle_\phi}{\sqrt{2}}$).
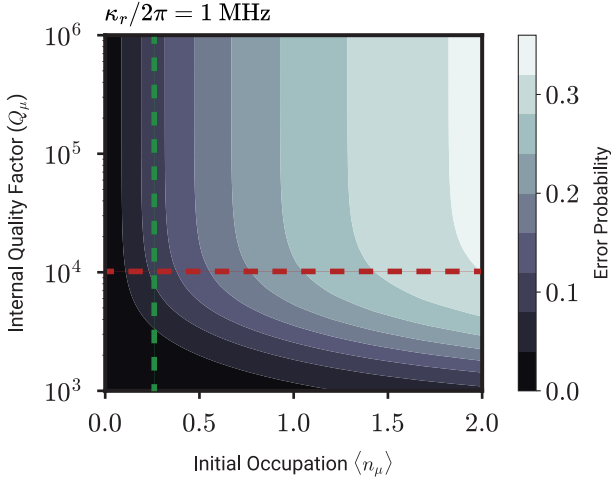
FIG. 6. **Dephasing error probability due to random decay of an excited parasitic mode, after PMIST, various internal parasitic quality factors.** The horizontal red line shows the quality factor quoted in [13]. The green line shows the dephasing error probability for transition 9 for various quality factors at $\kappa_r/2\pi = 1$ MHz (see Figs. 4(b) and 5).

A master equation simulation illustrates the resulting qubit dephasing due to this mechanism. We investigate a reduced system of the parasitic mode $\mu = 2$ and the fluxonium qubit (modeled as a two level system), interacting under the dispersive Hamiltonian $\hat{H}_\theta/\hbar = \chi_{\phi\mu}\hat{a}_\mu^\dagger\hat{a}_\mu\sigma_z$, and with a loss dissipator having collapse operator $\sqrt{\kappa_\mu}\hat{a}_\mu$, describing the parasitic mode internal loss. We start the system in a product state, where the parasitic mode has some initial non-zero occupation, and the qubit is in the pure state $|+\rangle$. We let the system evolve for a time $T_f = 10/\kappa_\mu$ long enough to allow the parasitic mode to relax, and then compute the fidelity of the final qubit state with the initial state $|+\rangle$, defining the error probability be the corresponding infidelity. This quantity is plotted in Fig. 6, both as a function of the initial parasitic mode occupancy $\langle n_\mu \rangle$ and its internal quality factor Q_μ. We present an illustrative calculation where we initialize the parasitic mode in a thermal state with average occupation number equal to $n_\mu \in [0,2]$. Note that results quoted for dephasing in the text below do not change significantly if the parasitic mode was instead initialized a coherent state $|\alpha\rangle$ such that $|\alpha|^2 = \langle n_\mu \rangle$. We find that for an internal quality factor Q_μ of 10^4, an initial population of $\langle n_\mu \rangle = 0.25$ in the parasitic mode introduces a dephasing error probability $\epsilon \sim 0.1$, which is already past the threshold of the surface code [36]. The explicit time-dependent simulations shown in Fig. 4 indicate that using a realistic readout power of ~ 10 photons, the final post-readout parasitic mode population is $\langle n_\mu \rangle \sim 0.25$. This population would already be enough to lead to a significant post-readout dephasing effect.

IV. EFFECTS OF CIRCUIT MODIFICATIONS ON PMIST

Let's explore how adjusting the qubit frequency, readout resonator frequency, and parasitic mode frequencies, may affect unwanted transitions. We rely on derivations in Ref. [26] for the circuit in Fig. 2, as well as generalizations introduced in App. A.

A. Coupling Strengths

Fig. 7 identifies the main culprit behind PMIST as the fluxonium-parasitic-mode coupling, $g_{\phi\mu}$. We compare the results of Floquet branch analyses for the initial state $|\tilde{1}, \tilde{0}\rangle$ under different coupling conditions, drive frequencies, and amplitudes. Fig. 7(a), reproduces as a reference the simulation results for our previous choice of coupling strengths $g_{\phi\mu}$ and $g_{\mu r}$. In contrast, Fig. 7(b) shows the same simulation but with $g_{\phi\mu}$ set to zero. We observe that a non-negligible $g_{\phi\mu}$ is the main reason for PMIST effects. This is evident from the absence of parasitic transitions $(8,9)$ in the top panel, and no streak or sharp change in color indicating parasitic mode excitations in the bottom panel: for $g_{\phi\mu} = 0$ the parasitic mode population always remains below $\langle n_\mu \rangle = 10^{-4}$.

Further, Fig. 7(c) shows that turning the parasitic-readout coupling to zero shows no reduction in PMIST. Thus, we can conclude that the qubit-readout coupling $g_{\phi r}$ alone does not cause significant transitions or PMIST processes without $g_{\phi\mu}$. Therefore, reducing the coupling strength $g_{\phi\mu}$ is a potential path to reducing the likelihood of PMIST processes.

Next, we analyze the dependence of these coupling strengths on circuit and readout parameters. As discussed, only even-index parasitic modes have a non-zero coupling to the qubit [26] (see derivation in App. A). The coupling strength $g_{\phi\mu}$ between an even parasitic mode and the qubit is given by

$$\frac{g_{\phi\mu}}{2\pi} = \frac{4}{\sqrt{2N}} \frac{\tilde{E}_c^\phi \tilde{E}_{c,\mu}^e c_\mu}{E_{\mathrm{g,j}} s_\mu^2} \cdot N_{\phi_{\mathrm{ZPF}}} \cdot N_{\mu_{\mathrm{ZPF}}}, \quad (9)$$

where $c_\mu = \cos\frac{\pi\mu}{2N}$, $s_\mu = \sin\frac{\pi\mu}{2N}$. $\tilde{E}_c^\phi, \tilde{E}_{c,\mu}^e$ are the qubit and even parasitic mode charging energies, respectively, and $N_{\phi/\mu,\mathrm{ZPF}}$ are the zero-point fluctuation values for the qubit and parasitic modes. $\tilde{E}_c^\phi, N_{\phi/\mu,\mathrm{ZPF}}$ are given in Apps. B 1, and

$$E_{c,\mu}^e = \left[\frac{1}{E_{C_j}} + \frac{1}{4E_{\mathrm{g,j}}s_\mu^2}\right]^{-1}. \quad (10)$$

All the other variables represent independent quantities listed in Table I.

We see that suppressing the parasitic capacitance to ground near the junction array suppresses the qubit-parasitic coupling $g_{\phi\mu}$. However, this is constrained by practical limitations to order $\mathcal{O}(0.1)$ fF per junction. The parasitic modes with the strongest coupling to the qubit have $\mu \ll N$. The large N, small μ limit with $c_\mu \approx 1$ yields

$$\tilde{E}_{c,\mu}^e \approx 4E_{\mathrm{g,j}}s_\mu^2, \quad \tilde{E}_c^\phi \propto \frac{1}{N^2} \implies g_{\phi\mu} \propto \frac{1}{N^{5/2}}. \quad (11)$$
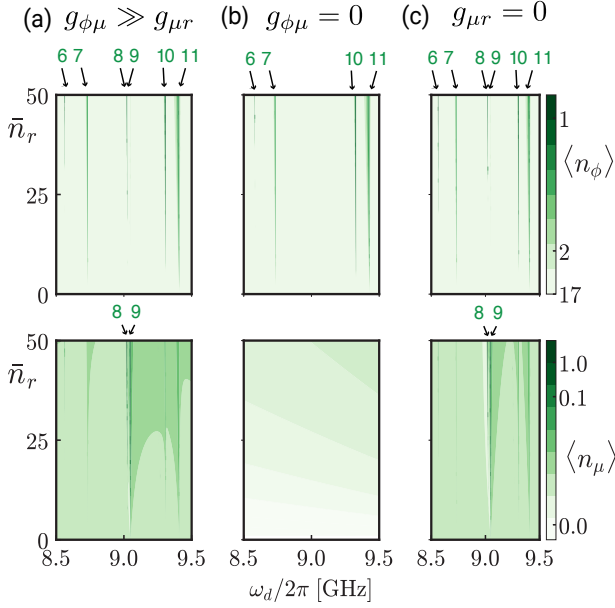
FIG. 7. **Sensitivity of PMIST processes to parasitic mode coupling strengths.** Panels show the result of Floquet branch analyses for the circuit parameters in Table I. MIST processes observed in Fig. 3 are labeled with numbers and indicated with arrows. **(a)** All parameters the same as Fig. 3(b). **(b)** Same, except now we set the parasitic mode to qubit coupling $g_{\phi\mu}$ to zero. Note that all PMIST features are now gone. **(c)** Same as (a), but we now set the parasitic mode to readout resonator coupling $g_{\mu r}$ to zero. As with previous Floquet branch analysis plots, color scales use a log scale scale to make transitions more visible.

These dependencies are plotted in Fig. 13 of App. B 1. We find that the coupling strength *decreases* with the number of junctions N, however, a limit to this increase may be set by the requirement of a constant inductance $E_L = E_{J_j}/N$ (see App. B 1).

B. Mode Frequencies

An alternate strategy is to tailor the circuit so that the resonance conditions required for PMIST are never realized. We can estimate these conditions by identifying energy-conserving processes, where x drive photons are converted into a transition with an energy difference $\tilde{\Delta}_{if,y}$ in the hybridized eigenspace of the fluxonium and parasitic mode $\mu = 2$. Here, $\tilde{\Delta}_{if,y}$ is the transition energy between levels $|\tilde{i}, \tilde{m}\rangle$ and $|\tilde{f}, \tilde{n}\rangle$ such that $|m - n| = y$. This equation can also be interpreted as a process where x readout photons convert into y parasitic mode photons and a fluxonium excitation $|i\rangle_\phi \leftrightarrow |f\rangle_\phi$ such that $\Delta_{if} = \hbar|\omega_f - \omega_i|$. To guide intuition for understanding the spectrum of resonance conditions, we plot such energy-conserving processes in Fig. 8 that involve the parasitic mode $\mu = 2$. We plot all processes that are *approximately* energy conserving within a window ϵ, i.e. that satisfy:

$$\left(|x\omega_r - \tilde{\Delta}_{if,y}/\hbar| = |x\omega_r - y\omega_\mu - \Delta_{if}/\hbar| \right) \le \epsilon. \quad (12)$$
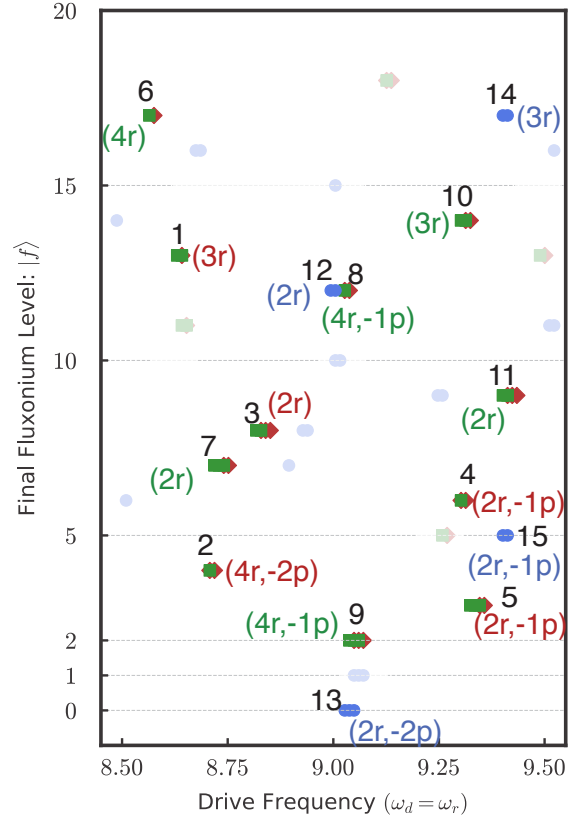

FIG. 8. **Energy conserving processes** $|\tilde{i}, \tilde{0}\rangle \leftrightarrow |\tilde{f}, \tilde{y}\rangle$ **for Eq. 12 with** $x \le 4, y \le 2, f \le 20$ **and** $i = 0$ **(red diamonds),** $i = 1$ **(green squares),** $i = 2$ **(blue circles).** The horizontal lines indicate the initial state i for visual aid. Labels in black correspond to transition # listed in Table III. The colored labels correspond to the disjoint subspaces for simplified representation but the energy conservation uses the eigen-energies of the hybridized eigenstates of H_0 (see Eq. 5). For example, the green label $(4r, -1p)$, for transition 8 of Table III, shows the number of readout photons absorbed (4) and the number of parasitic mode ($\mu = 2$) photons emitted (1) in the process. The faded points are weaker transitions not captured in the Floquet simulations.

We take a fairly liberal value of $\epsilon = 25$ MHz , to make sure we identify processes that could conceivably become resonant once Stark shifts due to the readout drive are accounted for (see App. C 3 a for details).

Fig. 8 depicts all four-photon processes that occur with approximate energy conservation, for drive frequencies within our target range, and when starting in one of the four lowest fluxonium levels. The results from Floquet simulations are shown in solid dots and labeled in black (see Sec. III), while the processes not identified in the simulation are faded. Note that there are downward transitions from $|2\rangle_\phi$ (blue dots) to the states $|1\rangle_\phi$ (green line) and $|0\rangle_\phi$ (red line) in the fluxonium subspace in the presence of parasitic modes. An example is captured by transition 14 of Table I.

The parenthesized labels in color denote the number of readout photons (xr) and parasitic mode photons (yp) required for the transition in the fluxonium subspace, where a positive index denotes absorption/de-excitation while a negative index de-

notes emission/excitation. For example, transition 2 corresponds to the emission of four readout photons, which are converted into two parasitic mode photons, absorbed by the mode $\mu = 2$, as well as an excitation from $|0\rangle_\phi$ to $|4\rangle_\phi$ in the fluxonium subspace.

Intuitively, many readout photons are required to bridge a large energy gap between the readout frequency and parasitic mode frequency. As this gap increases, the likelihood of PMIST processes decrease. We verify this intuition by considering the dependence on both the parasitic mode frequency and drive frequency in what follows.

a. Parasitic Mode Frequency: An approach towards mitigating PMIST processes is to adjust ω_μ so that $\omega_\mu \gg \omega_r$ for $\mu = 2$, requiring more readout photons to be absorbed in PMIST processes and therefore reducing PMIST transition rates. The dependence of the parasitic mode frequencies for even μ is

$$\frac{\omega_\mu^e}{2\pi} = \sqrt{8 E_{c,\mu}^e E_{J_j}} \tag{13}$$

See Eq. 10 for $E_{c,\mu}^e$ and Table I for E_{J_j}. Again, we focus on large N and small μ limit to focus on parasitic modes with the strongest coupling to the qubit. From derivations in Ref. [26] it is clear that parasitic frequency decreases with increase in junction count and parasitic ground capacitance. Thus, decreasing parasitic ground capacitance decreases both parasitic frequency and qubit-parasitic coupling. Increasing N on the other hand is only favorable for reducing the coupling strength while decreasing the gap between the between ω_d and ω_μ. The impact of decreasing N to increase this gap would require consideration of nonlinear corrections as well as fixed inductance, thus, making these changes difficult in practice [26].

b. Drive Frequency (ω_d): If, on the other hand, readout ($\omega_d \ll \omega_{\mu=2}$), a large readout photon number x would be needed while having a similar impact. We give the Floquet figure corresponding to a low-frequency readout regime in Fig. 9 which shows higher parasitic mode populations compared to our previous case in Fig. 3. The PMIST effects can be explained by examining the increased density of resonances when $\omega_d/2\pi \approx 6$ GHz. Note that this frequency is approximately the fluxonium plasma frequency $\omega_{12}/2\pi$ and is also half the parasitic mode $\mu = 2$ frequency. This introduces multiple frequency collisions, which cause the various transitions observed in the figure. This logic already indicates that $5.5 - 6$ GHz [37] would be a bad range of frequencies for the current choice of parameters. Formal transition probability calculations, same as Sec. III C, will be required to predict the how detrimental these effects can be. However, the energy conservation indicates that in spite of the increase in the number of PMIST effects, such transitions will be higher-order processes (large x) and thus suppressed for typical readout powers where $\bar{n}_r \sim \mathcal{O}(10^2)$ [16].

A high-frequency readout ($\omega_d \gg \omega_{\mu=N-1}$) case requires a large Hilbert space and is beyond the scope of this work [38].
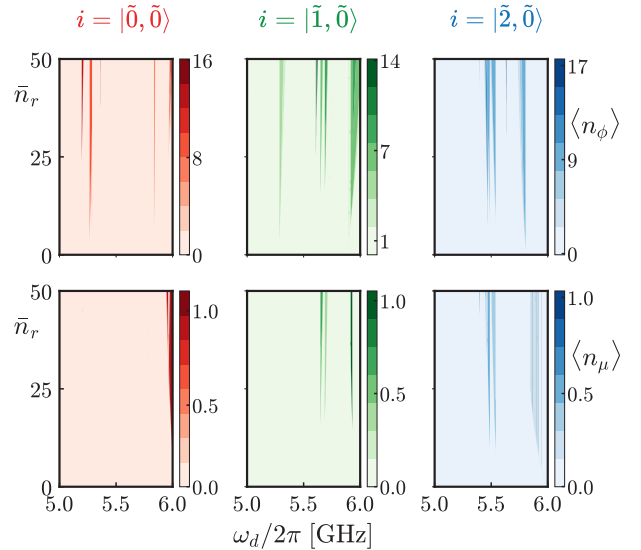

FIG. 9. **Floquet simulations at lower readout frequencies.** Circuit parameters used are the same as quoted in Tables I and II for branch analysis starting in the dressed hybridized eigenstate $i = |\tilde{k}, \tilde{0}\rangle$, with maximum overlap to the un-hybridized states $|k\rangle_\phi \otimes |0\rangle_{\mu=2}$. The figures are plotted in linear scale, unlike Fig. 3, making any streak due to significantly weaker transitions unnoticeable.

C. Alternative Circuit Parameters

Our analysis of PMIST so far has focused on systems where the fluxonium qubit frequency is $\omega_{01}/2\pi \sim 30$ MHz. Here, we consider how these processes change when one uses a larger qubit frequency $\omega_{01}/2\pi \sim 300$ MHz, as was recently realized in the experiment of Ref. [6] (see App. D for full circuit parameters). The parasitic mode frequency of the $\mu = 2$ mode is $\omega_{\mu=2}/2\pi = 15.50$ GHz. The coupling strengths are: $g_{\phi r}/2\pi = 37$ MHz, $g_{\phi\mu}/2\pi = 216$ MHz, $g_{\mu r}/2\pi = 6$ MHz. The plasma frequency is $\omega_{12}/2\pi = 5.40$ GHz. The assumptions for numerical modeling are the same as previous Floquet simulations as discussed in App. C 2. Even though the coupling strengths for these circuit parameters are similar to our previous parameter set in Table II, since the $\mu = 2$ parasitic mode mode is larger by about 4 GHz, we expect fewer PMIST processes for the drive frequency range analyzed in Fig. 3.

Fig. 10 shows that indeed, PMIST effects are comparatively less likely for this alternate circuit. The single PMIST process observed in the Floquet profile $|\tilde{0}, \tilde{0}\rangle \leftrightarrow |\tilde{4}, \tilde{1}\rangle$ occurs at $\bar{n}_r = 25$ and has the quasienergy gap of $\Delta_{ac} = 0.13$ MHz at the avoided crossing. The quasienergy gap at the avoided crossing for this transition is $\Delta_{ac} = 0.12$ MHz. The explicit transitions with quasienergies for the Floquet profile shown in Fig. 10(c) can be found in App. D. The overall reduced number of MIST effects in Fig. 10 compared to Fig. 3 is due to the faster decreasing charge matrix elements for this circuit (compare Fig. 18 with Fig. 14).

While the above results might seem promising, we remind the reader our work considers one particular avenue (lowest-frequency array mode with the
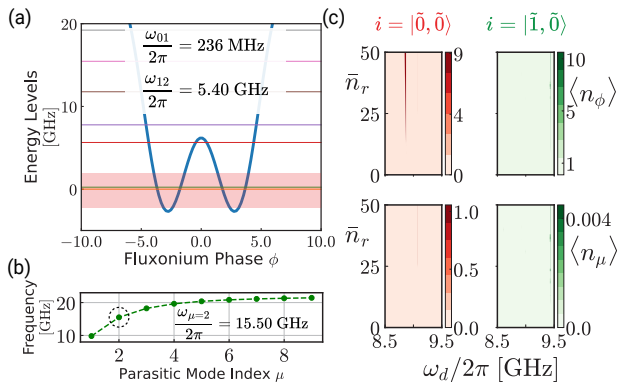
FIG. 10. **Floquet analysis with alternate JJA fluxonium parameters inspired by Ref. [6]. (a)** Fluxonium energy spectrum. **(b)** Parasitic mode frequencies. **(c)** Floquet simulations for the branch analysis of the computational states. Circuit parameters for this circuit are discussed in Sec. IV C and App. D. The Floquet figures are plotted in linear scale unlike Fig. 3, making any streak due to significantly weaker transitions unnoticeable.

strongest qubit-parasitic coupling) for the PMIST analysis shown here. This indicates the requirement of a detailed understanding of this Floquet profile, including rate calculations, is necessary to understand the relationship between fluxonium circuit parameters and the density of MIST effects.

V. CONCLUSION AND FURTHER WORK

In this work, we have analyzed the impact of parasitic modes on driven JJA fluxonium qubits, showing that measurement-induced state transitions of a fluxonium qubit can occur via excitations of a parasitic mode of the JJA. These processes, we have called PMIST, occur at particular resonance conditions when the energy of several readout photons is equal to a small number of parasitic mode excitations and a fluxonium mode excitation.

We find that PMIST transitions can occur at meaningfully-high rates (with avoided crossing quasienergy gap $\Delta_{ac} = 0.66$ MHz) because of the strong coupling between parasitic modes and the qubit. Consequently, it is possible to have qubit state transitions mediated via JJA internal mode during fluxonium readout, even at low average readout photon numbers and while using typical parameters that enable high fidelity, dispersive readout. For example, we have shown that PMIST does lower the onset of MIST processes to ~ 10 readout photons at certain drive frequencies. In addition, it has the potential to significantly dephase the qubit post-measurement, which could in turn limit the qubit gate fidelities required for quantum error correction, and ultimately the performance of a quantum processor. However, the coupling of the parasitic mode to the readout is still sufficiently weak such that, for the vast majority of readout frequencies, the JJA mode excitation population is negligible unless a PMIST occurs. Therefore, these processes can be avoided via judicious choice

of readout, junction array, and fluxonium parameters. We analyze the trend in PMIST for various drive frequencies, parasitic mode frequencies, coupling constants, and circuits with two different qubit frequencies equal to ~ 30 and ~ 300 MHz.

We have presented a first analysis toward understanding the role of parasitic modes in the dispersive readout dynamics of a fluxonium circuit. Mitigating the parasitic mode excitations could involve careful selection of the readout resonator frequency, and varying junction energies along the array to localize parasitic modes. Such modifications alter the parasitic mode spectrum towards reducing excitation probability. The circuit parameters used in this work correspond to a parasitic mode of the fluxonium's junction array. However, other modes with similar frequencies may also participate in the environment of the fluxonium. This may include, for example, confined package modes, slot line modes, and harmonics of coplanar waveguide resonators for readout. Our results show the significance of taking all such modes into consideration when driving many excitations into highly nonlinear circuits.

Appendix A: Single-Point Connections

Parameters	Variables	Values
Phase-slip JJ capacitance	C_p	13.3 fF
Differential capacitance	C	1.14 fF
JJA capacitance energy	C_j	26.2 fF
JJA ground capacitance	$C_{g,j}$	0.1 fF
Phase-slip ground capacitance	$C_{g,p}$	10 fF
Coupling capacitance	C_c	1 fF
ZPF of the resonator/drive	V_{ZPF}	0.75 GHz
ZPF of fluxonium charge operator	$N_{\phi,ZPF}$	0.36
ZPF of parasitic charge operator	$N_{\mu=2,ZPF}$	1.58

TABLE IV. Capacitances and zero-point fluctuation (ZPF) values for the fluxonium readout circuit used in the main text in Figs. 2 and 11(a).

The fluxonium readout circuit shown in Fig. 2 of main text can have several modifications, each of which may affect various performance metrics. This circuit has a parallel configuration with a symmetry (identified in Ref. [29]) which removes the coupling to
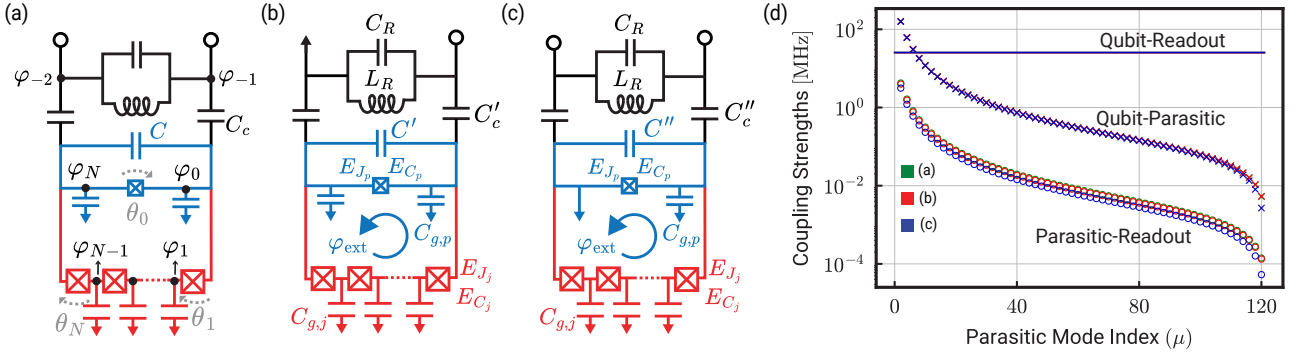
FIG. 11. (a-c) Alternative readout circuits. (a) Parallel circuit (H_1) same as Fig. 2(a), (b) Floating fluxonium (H_2), (c) Grounded fluxonium (H_3). Alternatives (b) and (c) require a single-point connection to the readout line V, unlike the parallel circuit in (a). The parallel circuit is used as a reference for denoting phase variables φ_i at each node and phase difference variables θ_j across each junction used in the derivation of the Lagrangian for all three circuits. We maintain the values for all circuit variables the same except for the coupling capacitances C, C', C'' and differential capacitances C_c, C_c', C_c''. (d) Absolute values of the coefficients of coupling terms in the Hamiltonian (in GHz). We can see that some parasitic modes couple to the qubit stronger than the qubit couples to the readout for all three circuits. The parasitic mode coupling to the readout is very slightly weaker in H_3 compared to H_1, H_2.

the lowest frequency mode $\mu = 1$ [26]. The elements crucial to this symmetry are the equal coupling capacitances on both ends of the parallel circuit. While preserving this symmetry, in Fig. 11, we present two modifications to the parallel circuit, with different grounding options for the fluxonium and the resonator. We will refer to these circuit choices as: H_1, parallel circuit in Fig. 11(a) (same as Fig. 2), H_2, grounded resonator circuit in Fig. 11(b), and H_3, grounded fluxonium circuit in Fig. 11(c). The second modification is used to study the readout fidelity in case of a hangar geometry with a single voltage line. The third modification is used to study the differences between a floating fluxonium circuit and a grounded fluxonium circuit in terms of readout. We adjust the coupling capacitances (using $C_{c'} = 5.06$ fF, $C_{c'}' = 4.12$ fF in Figs. 11(b,c)) and the total capacitance of the phase slip junction (busing $C' = 4.97$ fF, $C'' = 5.8$ fF in Fig. 11(b,c)), as compared to the values for the parallel circuit given by Table IV. These modifications achieve the same qubit frequency $\omega_{01}/2\pi$, plasmon frequency $\omega_{12}/2\pi$, qubit-readout coupling constant $g_{\phi\mu}$ and qubit-readout dispersive shift $\chi_{\phi r}$ for the three circuits as given by Table II. Under these choices, we find that the readout parameters affected by parasitic modes are roughly the same across all three circuits, given our assumptions of ordered array and no self-nonlinearity in parasitic modes. See Table V in App. B for details.

1. Lagrangian

We will first derive the Lagrangians for the circuits in Figs. 11(a-c) to be used in the next section for comparison. To do this, we follow the recipe given in Refs. [26, 29] for the parallel circuit. To this, we shall impose the modifications and thence derive the Lagrangians for circuits 11(b,c). Importantly, we will show that the symmetry in the parallel circuit which prevents any coupling with the lowest-frequency para-

sitic mode ($\mu = 1$) is preserved in all three circuits, absence of which would have changed the Floquet landscape across the three circuits significantly.

The Lagrangian corresponding to these circuits is a combination of the Lagrangians, $\mathcal{L}_{\text{phase-slip}}$ from the phase-slip junction shown in blue (comprising of the junction with $E_J/E_C \sim 5 - 8$ and the capacitor C), $\mathcal{L}_{\text{JJA}}$ from the (red) junctions in the array, $\mathcal{L}_{\text{g}}$ from the ground capacitances, $\mathcal{L}_{\text{R}}$ from the readout resonator and $\mathcal{L}_{\text{c}}$ due to the coupling capacitances C_c. The node flux variables at various points in the circuit are denoted by $\varphi_i = 2\pi\Phi_i/\Phi_0$. We mark the phase-difference across the junctions in the array, $\theta_i = \varphi_i - \varphi_{i-1}$, and across the phase-slip junction, $\theta_0 = \varphi_N - \varphi_0$, as shown in Figs. 11(b,c). Similarly, the voltage drop across each junction is given by the phase evolution equation $\dot{\theta}_i = \dot{\varphi}_i - \dot{\varphi}_{i-1} = 2\pi V_i/\Phi_0$ where $\Phi_0 = h/2e$ the superconducting flux quantum. We will use subscripts j, p for JJA and the phase-slip junction coordinates, respectively. For the Lagrangian for the parallel circuit [26, 29] (setting $\hbar = 1$), we have,

$$\mathcal{L} = \mathcal{L}_{\text{phase-slip}} + \mathcal{L}_{\text{JJA}} + \mathcal{L}_{\text{g}} + \mathcal{L}_{\text{R}} + \mathcal{L}_{\text{C}}. \quad \text{(A1)}$$

where

$$\mathcal{L}_{\text{phase-slip}} = \frac{1}{16E_{C'}}(\dot{\varphi}_N - \dot{\varphi}_0)^2 - E_{J_p}\cos\Big(\sum_{i=1}^{N}\theta_i + \varphi_{\text{ext}}\Big) \quad \text{(A2)}$$

$$\mathcal{L}_{\text{JJA}} = \sum_{i=1}^{N}\frac{1}{16E_{C_j}}(\dot{\varphi}_i - \dot{\varphi}_{i-1})^2 - E_{J_j}\cos(\theta_i) \quad \text{(A3)}$$

$$\mathcal{L}_{\text{R}} = \frac{1}{16E_{C_R}}(\dot{\varphi}_{-1} - \dot{\varphi}_{-2})^2 + \frac{1}{16E_{L_R}}(\varphi_{-1} - \varphi_{-2})^2 \quad \text{(A4)}$$

$$\mathcal{L}_{\text{g}} = \sum_{i=1}^{N-1}\frac{\dot{\varphi}_i^2}{16E_{\text{g,j}}} + \sum_{i=0,N}\frac{\dot{\varphi}_i^2}{16E_{\text{g,p}}} \quad \text{(A5)}$$

$$\mathcal{L}_{\text{c}} = \frac{1}{16E_{c'}}(\dot{\varphi}_{-1} - \dot{\varphi}_0)^2 + \frac{1}{16E_{c'}}(\dot{\varphi}_{-2} - \dot{\varphi}_N)^2$$

$$= \frac{\dot{\varphi}_0^2}{16E_{c'}} + \frac{\dot{\varphi}_{-1}^2}{16E_{c'}} - \frac{\dot{\varphi}_0\dot{\varphi}_{-1}}{8E_{c'}}. \tag{A6}$$

The definitions and values of capacitive energies used here are given in Table I except for $E_{C'} = e^2/2C'$. Here the terms associated with $\dot{\varphi}_i(\theta_i)$ are the kinetic (potential) energy terms. We can ignore the harmonic oscillator Lagrangian $\mathcal{L}_R$ due to triviality. We will now expand on the derivation in Refs. [26, 29] for completeness.

We can use the definition of phase difference quadratures

$$\varphi_m - \varphi_0 = \sum_{l=1}^{m} \theta_l \tag{A7}$$

and the fluxoid quantization with an external flux choice of $\varphi_{\text{ext}} = \pi$ as per the main text.

$$\sum_{m=0}^{N} \theta_m + \varphi_{\text{ext}} = 2\pi z, \tag{A8}$$

where $z \in \mathbb{Z}$ is an arbitrary integer. Writing the the Lagrangian in this new basis follows $\partial\mathcal{L}/\partial\dot{\varphi}_0 = 0$ yields the expression,

$$\dot{\varphi}_0 = E_t\left(\frac{\dot{\varphi}_{-1}}{E_{c'}} - \sum_{l=1}^{N} \frac{\dot{\theta}_l}{E_{g,p}} - \sum_{i=1}^{N-1}(N-i+1)\frac{\dot{\theta}_i}{E_{g,j}}\right) \tag{A9}$$

where

$$E_t = \left(\frac{1}{E_{c'}} + \frac{N-1}{E_{g,j}} + \frac{2}{E_{g,p}}\right)^{-1} \tag{A10}$$

is the total capacitive energy of the circuit due to the parasitic and coupling capacitances.

$$\therefore \mathcal{L}_g + \mathcal{L}_c = \frac{\dot{\varphi}_{-1}^2}{16E_{c'}}\left(1 - \frac{E_t}{E_{c'}}\right)$$
$$+ \left[\frac{E_t}{E_{g,p}}\dot{\theta}_N + \sum_{i=1}^{N-1}(N-i+1)\frac{E_t}{E_{g,j}}\dot{\theta}_i\right]\frac{\dot{\varphi}_{-1}}{8E_{c'}}$$
$$- \sum_{i=1}^{N}\sum_{i'=1}^{N} \frac{\dot{\theta}_i\dot{\theta}_{i'}}{16E_{g,p}}\left(1 + \frac{E_t}{E_{g,p}}\right)$$
$$+ \sum_{i=1}^{N-1}\sum_{i'=1}^{N-1} \frac{\dot{\theta}_i\dot{\theta}_{i'}}{16E_{g,j}}\left(\sum_{j=\max\{m,n\}}^{N}\frac{1}{16E_g}\right)$$
$$\times \left(1 - \sum_{i=\min\{m,n\}}^{N}\frac{E_t}{E_g}\right) \tag{A11}$$

We simplify the Lagrangian $\mathcal{L}_g + \mathcal{L}_c$ as

$$= \sum_{m=1}^{N}\sum_{n=1}^{N} \dot{\theta}_m\dot{\theta}_n \frac{(N-\max\{m,n\}+1)\min\{m,n\}E_t}{16E_g^2} \tag{A12}$$

The first line shows that the contribution from the coupling capacitance comes only via the readout resonator mode. The second and third lines, on the other hand, show the terms which contribute to parasitic couplings via the the ground capacitance due to terms proportional to $\dot{\theta}_m\dot{\theta}_n$.

Note that for the grounded resonator and grounded fluxonium circuits, see Figs. 11(b,c), we can respectively impose $\dot{\varphi}_{-2} = 0$ and $\dot{\varphi}_N = 0$.

a. Collective Modes. Now, we will define the collective modes for the fluxonium circuit, $\{\phi, \xi_1, ..., \xi_{N-1}\}$ such that

$$\theta_m = \phi/N + \sum_\mu W_{\mu m}\xi_\mu, \tag{A13}$$

and inversely,

$$\phi = \sum_m \theta_m, \quad \xi_\mu = \sum_m W_{\mu m}\theta_m. \tag{A14}$$

Here, ϕ is called the superinductance mode or the *qubit* mode while ξ_μ denote the parasitic modes indexed by $\mu \in \{1, .., N-1\}$ [29]. The matrix W is semi-orthogonal, with dimensions $(N-1) \times N$, and is given by $\sum_m W_{\mu m}W_{\nu m} = \delta_{\mu\nu}$. Its row sum is zero, $\sum_m W_{\mu m} = 0$. Thus, the following choice

$$W_{\mu m} = \sqrt{\frac{2}{N}}\cos\frac{\pi\mu(m-1/2)}{N}, \tag{A15}$$

is observed in [29] and later used in [26] to derive the Hamiltonian for the parallel circuit. The choice of these new variables highlights the collective modes describing the low-energy physics as illustrated in [27, 39, 40]. We can now split the combined Lagrangian $\mathcal{L} = \mathcal{T} - \mathcal{U}$ into kinteic energy $\mathcal{T}$ and potential energy $\mathcal{U}$ terms in the basis of collective modes as, [SS: Here on, we need to remove terms due to Ec3 and Ec4, and also point out where the symmetry from the odd modes is coming from. We also need to separate Egj and Egp]

$$\mathcal{T} = \frac{\dot{\varphi}_{-1}^2}{16E_{c'}}\left(1 - \frac{E_t}{E_{c'}}\right) + \frac{1}{E_{c'}}\left(1 - \frac{E_t}{E_{c'}}\right)$$
$$+ \left[\sum_{n=1}^{N}\left(\frac{\dot{\varphi}_{-1}}{E_c} + \frac{\dot{\varphi}_{-2}}{E_c}\right)\left(\frac{E_t}{8E_c} + (N-n+1)\frac{E_t}{8E_g}\right)\right.$$
$$\left. - \sum_{n=1}^{N}\frac{\dot{\varphi}_{-2}}{8E_c}\right]\left(\dot{\phi}/N + \sum_\mu W_{\mu n}\dot{\xi}_\mu\right) + \sum_{m=1}^{N}\sum_{n=1}^{N}\left(\dot{\phi}/N\right.$$
$$+ \sum_\mu W_{\mu n}\dot{\xi}_\mu)(\dot{\phi}/N + \sum_\mu W_{\mu m}\dot{\xi}_\mu)\left((N - \max\{m,n\}\right.$$
$$+ 1)\frac{1}{16E_g} + \frac{1}{16E_c}\right)\left(\min\{m,n\}\frac{E_t}{E_g} + \frac{E_t}{E_c}\right) \tag{A16}$$

$$\mathcal{U} = -E_{J_p}\cos(\phi) - \frac{(\varphi_{-1} - \varphi_{-2})^2}{16E_R}$$
$$- \sum_{n=1}^{N} E_{J_j}\cos\left(\phi/N + \sum_\mu W_{\mu n}\xi_\mu\right) \tag{A17}$$

b. Symmetries in the Lagrangian   Simplifying the kinetic energy term from Eq. A16, recalling that $\sum_m W_{\mu m} = 0$, and the semi-orthogonal matrix condition $\sum_m W_{\mu m}W_{\nu m} = \delta_{\mu\nu}$ yields

$$\mathcal{T} = -\frac{\dot{\varphi}_{-2}eV}{16E_{c'}} + \frac{\dot{\varphi}_{-1}eV}{16E_{c'}} - E_t\frac{\dot{\varphi}_{-1}\dot{\varphi}_{-2}}{16E_{c'}^2}$$
$$+ \frac{\dot{\varphi}_{-1}^2}{16}\left(\frac{1}{E_c}\left(1 - \frac{E_t}{E_c}\right) + \frac{1}{E_c}\right) \tag{A18}$$

$$+ \frac{\dot{\varphi}_{-2}^2}{16}\left(\frac{1}{E_c} + \frac{1}{E_c}\left(1 - \frac{E_t}{E_c}\right)\right)$$

$$+ \frac{E_t}{8E_c^2}\dot{\varphi}_{-1}\dot{\phi} + \frac{E_t}{8E_c^2}\dot{\varphi}_{-2}\dot{\phi}$$

$$+ \Big[\sum_{n=1}^{N}\left(\frac{\dot{\varphi}_{-1}}{E_c} + \frac{\dot{\varphi}_{-2}}{E_c}\right)\left(\frac{E_t}{8E_c} + (N-n+1)\frac{E_t}{8E_g}\right)$$

$$- \sum_{n=1}^{N}\frac{\dot{\varphi}_{-2}}{8E_c}\Big]\Big(\dot{\phi}/N + \sum_\mu W_{\mu n}\dot{\xi}_\mu\Big)$$

$$+ \Big[(M_{00} + G_{00})\dot{\phi}^2 + 2\sum_\mu(M_{0\mu} + G_{0\mu})\dot{\phi}\dot{\xi}_\mu$$

$$+ \sum_{\mu,\nu}(M_{\mu\nu} + G_{\mu\nu})\dot{\xi}_\mu\dot{\xi}_\nu\Big], \tag{A19}$$

where the coefficients are given by

$$M_{00} = \frac{1}{16E_{C'}} + \frac{1}{16NE_{C_j}}, \quad M_{0\mu} = 0, \quad M_{\mu\nu} = \frac{\delta_{\mu\nu}}{16E_{C_j}} \tag{A20}$$

$$G_{00} = \frac{1}{64E_t}\left(1 - \frac{E_t}{E_c}\right)^2\left[1 - \frac{2}{3}\frac{N-1}{N}\right] \tag{A21}$$

$$G_{0\mu} = -\frac{c_\mu o_{\mu+1}}{16E_g\sqrt{2N}s_\mu^2}\left(1 - \frac{E_t}{E_c}\right) \tag{A22}$$

$$G_{\mu\nu} = \frac{1}{64E_g s_\mu^2}\Big[\delta_{\mu\nu} - \frac{E_t}{E_g}\frac{2c_\mu c_\nu o_\mu o_\nu}{N s_\nu^2}\Big]. \tag{A23}$$

[SS: Define c,o.] The quantities $G_{00}, G_{0\mu}, G_{\mu\nu}$ contribute to the equations for coupling strengths while $M_{00}, M_{\mu\nu}$ contribute to the charging energies of the qubit and parasitic modes, discussed in Sec. IV. Note that G_{00} increases quadratically with a factor of $\left(1 - \frac{E_t}{E_c}\right)$. Thus, $G_{0\mu}$ is different from the parallel circuit by a factor $\left(1 - \frac{E_t}{E_c}\right)$. The last term, $G_{\mu\nu}$ same as the case of parallel circuit quoted in Ref. [26] because it has no dependence on coupling capacitances.

c. Linear Approximation From here on, we define a sum over m, n as running from 1 to N, while the sum over μ, ν runs from 1 to $N-1$. Simplification to including only linear terms from Taylor expansion of the cosine ($\cos x \sim 1 - \frac{x^2}{2}$) Eq. A17 and using $\sum_n W_{\mu m}W_{\nu m} = \delta_{\mu\nu}$, yields (up to a constant term)

$$\mathcal{U} = E_{J_p}\cos(\phi) - \frac{(\varphi_{-1} - \varphi_{-2})^2}{16E_R}$$

$$+ \frac{E_{J_j}}{2N}\phi^2 + \frac{E_{J_j}}{2}\sum_\mu\xi_\mu^2 \tag{A24}$$

$$= E_{J_p}\cos(\phi) + \frac{E_{J_j}}{2N}\phi^2 + \frac{E_{J_j}}{2}\sum_\mu\xi_\mu^2 - \frac{\varphi_-^2}{16E_R}, \tag{A25}$$

where $\dot{\phi}_{-1} = -\dot{\phi}_{-2} = eV$ [SS: Need to remove eV in this derivation]

We can see that there is no choice of $\dot{\varphi}_\pm$ such that the parasitic coupling between the readout resonator and fluxonium can be canceled without eliminating the coupling between the qubit and readout resonator. Note that, $\frac{N+1}{E_g} = \frac{1}{E_g} - \frac{1}{E_c}$ [SS: weird!], and thus, the

coupling between the qubit and the readout is same as the parallel circuit if $E_g \ll E_c$ with a lower N. We drive the readout resonator, such that, $\dot{\varphi}_- \equiv 2eV$ (the sign of the voltage value has been changed because in this circuit φ_{-1} will be connected to V and not $-V$, just for simplicity).

$$\mathcal{L} = \frac{\dot{\varphi}_+^2}{64E_c}\left(2 + \frac{(N+1)E_t}{E_g}\right) + \frac{\dot{\varphi}_+ eV}{16E_c}\left(\frac{3}{2} + \frac{E_t}{E_c}\right)$$

$$- \frac{(N+1)E_t}{32E_g E_c}\dot{\phi}eV + \frac{(N+1)E_t}{64E_g E_c}\dot{\phi}\dot{\varphi}_+$$

$$- \frac{E_t}{16E_g E_c}\sum_\mu\frac{c_\mu o_\mu}{\sqrt{2N}s_\mu^2}\dot{\xi}_\mu eV$$

$$+ \frac{E_t}{32E_g E_c}\sum_\mu\frac{c_\mu o_\mu}{\sqrt{2N}s_\mu^2}\dot{\xi}_\mu\dot{\varphi}_+ + \mathcal{O}(e^2 V^2)$$

$$+ \Big[(M_{00} + G_{00})\dot{\phi}^2 + 2\sum_\mu(M_{0\mu} + G_{0\mu})\dot{\phi}\dot{\xi}_\mu$$

$$+ \sum_{\mu,\nu}(M_{\mu\nu} + G_{\mu\nu})\dot{\xi}_\mu\dot{\xi}_\nu\Big] - \mathcal{U} \tag{A26}$$

[SS: Correct the derivation in numerics and text to only use grounded resonator and then extend briefly to the floating case. We are ding so by eliminating all terms with E_c^3, E_c^4 and using $\dot{\varphi}_{-2} = 0, \dot{\varphi}_{-1} = -2eV$. Thus, $\varphi_+ = \varphi_- = -2eV$. So this point everything will be correct and we do not need to change the equations for Ec but only for Eg]

$$= -\frac{(N+1)E_t}{16E_g E_c}\dot{\phi}eV - \frac{E_t}{8E_g E_c}\sum_\mu\frac{c_\mu o_\mu}{\sqrt{2N}s_\mu^2}\dot{\xi}_\mu eV$$

$$+ \Big[(M_{00} + G_{00})\dot{\phi}^2 + 2\sum_\mu(M_{0\mu} + G_{0\mu})\dot{\phi}\dot{\xi}_\mu$$

$$+ \sum_{\mu,\nu}(M_{\mu\nu} + G_{\mu\nu})\dot{\xi}_\mu\dot{\xi}_\nu\Big] - \mathcal{U} \tag{A27}$$

d. Hamiltonian: We will now use Legendre transformation to obtain Hamiltonian variables,

$$p_\phi = \frac{\partial\mathcal{L}_{\mathcal{K}o}}{\partial\dot{\phi}} = 2(M_{00} + G_{00})\dot{\phi} + \sum_\mu(M_{\mu 0} + G_{\mu 0})\dot{\xi}_\mu$$

$$- \frac{(N+1)E_t}{16E_g E_c}eV \tag{A28}$$

$$p_{\xi_\mu} = \frac{\partial\mathcal{L}_{\mathcal{K}o}}{\partial\dot{\xi}_\mu} = (M_{0\mu} + G_{0\mu})\dot{\phi} + 2\sum_\nu(M_{\mu\nu} + G_{\mu\nu})\dot{\xi}_\nu$$

$$- \frac{E_t}{8E_g E_c}\sum_\mu\frac{c_\mu o_\mu}{\sqrt{2N}s_\mu^2}eV \tag{A29}$$

[SS: define odd and even sectors and then check what is different here.] Here, the even and odd sectors are not decoupled due to the eV term. The even and odd sectors can be diagonalized independently, such that a rotation on the odd sectors does not affect the even sectors. This is contrary to the case of Eq. 77 in [26] where the rotation of odd sectors affects the even sectors. This is because in that case $G_{0\mu}$ was changed to being dependent on odd as well as even sectors. However, here, only the $\mathcal{L}_V$ term has changed.

Thus, if the following condition is satisfied,

$$\frac{\tilde{E}_c^\phi \tilde{E}_{c,j}^e c_i c_j}{32 N E_{\rm g}^2 s_i^2 s_j^2} << 1 \implies \frac{4 E_{\rm g} \tilde{E}_c^\phi c_i c_j}{32 N E_{\rm g}^2 s_i^2} << 1 \quad \text{(A30)}$$

$$\implies \frac{4 \tilde{E}_c^\phi N}{8 E_{\rm g} \pi^2 \mu \nu} << 1 \implies N << 8\pi^2 \frac{E_{\rm g}}{\tilde{E}_c^\phi}, \quad \text{(A31)}$$

[SS: quote the N] we can carry out the exact same procedure as Ref. [26] to simplify the inversion of matrix for the Legendre transformation and obtain the Hamiltonian as follows. Thus, we arrive at the following Hamiltonian

$$
\begin{aligned}
H_2 =\ & 4 \bar{E}_c^\phi p_\phi^2 + \sum_{\mu=1}^{N-1} 4 \tilde{E}_{c,\mu}^{e/o} p_\mu^2 \\
& + 2 \sum_{\mu=1}^{N-1} \frac{\bar{E}_c^\phi \tilde{E}_{c,\mu}^{e/o} c_\mu o_{\mu+1}}{\sqrt{2N} E_{\rm g} s_\mu^2} p_\phi p_\mu \\
& - \bar{E}_c^\phi p_\phi e V \Big[\frac{(N+1) E_{\rm t}}{2 E_{\rm g} E_{\rm c}} + \frac{E_{\rm t}^2 \tilde{E}_{c,\mu}^{e/o}}{8 E_{\rm g}^2 E_{\rm c}^2} \Big(\frac{c_\mu^2 o_\mu}{2 N s_\mu^4} \Big) \Big] \\
& - \sum_{\mu=1}^{N-1} \frac{\bar{E}_c^\phi \tilde{E}_{c,\mu}^{e/o} c_\mu o_{\mu+1}}{\sqrt{2N} E_{\rm g} s_\mu^2} \Big[\frac{(N+1) E_{\rm t}}{8 E_{\rm g} E_{\rm c}} \Big] p_\mu e V \\
& + E_{J_{\rm p}} \cos \phi + \frac{E_L}{2} \phi^2 + \frac{E_{J_{\rm j}}}{2} \sum_{\mu=1}^{N-1} \xi_\mu^2 - \frac{\varphi_-^2}{16 E_R}
\end{aligned}
$$
(A32)

[SS: Connect this Hamiltonian to the original Hamiltonian and give the expression for each term.] where the variables $\tilde{E}_{c,\mu}^e$ are the same as before and $\tilde{E}_{c,\mu}^o$ is the diagonalized charging energy of odd sectors. Here, $\tilde{E}_{c,\mu}^{e/o}$ denotes that the term will be $\tilde{E}_{c,\mu}^o$ for odd μ and $\tilde{E}_{c,\mu}^e$ for even μ. Thus, we can see that by not preserving the symmetry we only have the extra odd sector term interacting with the readout resonator. However, this term is extremely small [ER: proportional to / why small]. Additionally, $\mathcal{U}$ remains the same as the parallel case. Thus, in terms of types of couplings there might not be major differences, however, the value of $\bar{E}_c^\phi = (G_{00} + M_{00})^{-1}$ changes since G_{00} has changed. This change can also be diminished with increasing N. Thus, for large enough N, this circuit is the same as the parallel circuit.

2. Grounded Fluxonium Circuit

[SS: only express initial Lagrangian upto showing the symmetry is preserved and then show the Hamiltonian] For H_3, the constraint $\dot{\varphi}_N = 0$ yields

$$\mathcal{L} = \mathcal{L}_{phase-slip} + \mathcal{L}_{JJA} + \mathcal{L}_g + \mathcal{L}_R + \mathcal{L}_C$$
(A33)

$$\mathcal{L}_{phase-slip} = \frac{\dot{\varphi}_0^2}{16 E_{\rm C'}} - E_{J_{\rm p}} \cos(\varphi_0 + \varphi_{\rm ext}) \quad \text{(A34)}$$

$$\mathcal{L}_{JJA} = \sum_{n=1}^N \frac{(\dot{\varphi}_n - \dot{\varphi}_{n-1})^2}{16 E_{C_j}^n} - E_{J_j}^n \cos(\varphi_n - \varphi_{n-1})$$
(A35)

$$\mathcal{L}_R = \frac{\dot{\varphi}_-^2}{16 E_R} - \frac{\varphi_-^2}{16 E_R} \quad \text{(A36)}$$

$$\mathcal{L}_g = \sum_{n=0}^{N-1} \frac{\dot{\varphi}_n^2}{16 E_g^n} \quad \text{(A37)}$$

Here, we will not assume that the capacitances to transmission line are infinite or that ground capacitance for the phase-slip junction and JJA. We will leave the value of $\varphi_\pm$ a variable in this case unlike the parallel circuit study we performed above. The grounding of fluxonium yields an additional condition to the fluxoid condition $\varphi_N = c$, a constant which implies that

$$\varphi_0 = c - \sum_{l=1}^N \theta_l \implies \dot{\varphi}_0 = - \sum_{l=1}^N \dot{\theta}_l \quad \text{(A38)}$$

This used to be our qubit in the definition of collective modes in this article. However, in this case there are only $N-1$ modes, such that the collective modes are defined as,

$$\phi = c + \sum_{l=1}^{N-1} \theta_l \implies \dot{\phi} = - \dot{\varphi}_0 \quad \text{(A39)}$$

Since one of the dynamic variables are fixed we only have $N-1$ modes, thus,

$$\mathcal{L}_{phase-slip} = \frac{(\sum_{m=1}^{N-1} \dot{\theta}_m)^2}{16 E_{\rm C'}} + E_{J_{\rm p}} \cos \Big(\sum_{m=1}^N \theta_m + \varphi_{\rm ext} \Big)$$
(A40)

$$\mathcal{L}_{JJA} = \sum_{n=1}^{N-1} \frac{\dot{\theta}_n^2}{16 E_{C_j}^n} - E_{J_j}^n \cos \theta_n \quad \text{(A41)}$$

$$\mathcal{L}_R = \frac{(\dot{\varphi}_{-1} - \dot{\varphi}_{-2})^2}{16 E_R} - \frac{(\varphi_{-1} - \varphi_{-2})^2}{2 L_R} \quad \text{(A42)}$$

$$\mathcal{L}_g = \frac{\dot{\varphi}_0^2}{16 E_g^0} + \sum_{n=1}^N \frac{(\dot{\varphi}_0 + \sum_{m=1}^n \dot{\theta}_m)^2}{16 E_g^m} \quad \text{(A43)}$$

$$
\begin{aligned}
=\ & \frac{\dot{\varphi}_0^2}{16 E_g^0} + \sum_{n=1}^N \frac{1}{16 E_g^n} \Big(\dot{\varphi}_0^2 + 2 \dot{\varphi}_0 \sum_{m=1}^n \dot{\theta}_m \\
& + \sum_{i=1}^n \sum_{j=1}^n \dot{\theta}_i \dot{\theta}_j \Big)
\end{aligned}
$$
(A44)

$$
\begin{aligned}
=\ & \dot{\varphi}_0^2 \sum_{n=0}^N \frac{1}{16 E_g^n} + 2 \sum_{n=1}^N \sum_{m=1}^n \frac{\dot{\varphi}_0 \dot{\theta}_m}{16 E_g^n} \\
& + \sum_{n=1}^N \sum_{j=1}^n \sum_{i=1}^n \frac{\dot{\theta}_i \dot{\theta}_j}{16 E_g^n}
\end{aligned}
$$
(A45)

$$
\begin{aligned}
\mathcal{L}_c =\ & \frac{\dot{\varphi}_0^2}{16 E_c^1} + \frac{\dot{\varphi}_{-1}^2}{16} \Big(\frac{1}{E_c^1} + \frac{1}{E_c^3} \Big) \\
& + \frac{\dot{\varphi}_{-2}^2}{16} \Big(\frac{1}{E_c^4} + \frac{1}{E_c^2} \Big) + \frac{(\dot{\varphi}_0 + \sum_{m=1}^N \dot{\theta}_m)^2}{16 E_c^2} \\
& - \frac{\dot{\varphi}_0 \dot{\varphi}_{-1}}{8 E_c^1} - \frac{\dot{\varphi}_{-2}(\dot{\varphi}_0 + \sum_{m=1}^N \dot{\theta}_m)}{8 E_c^2} \\
& - \frac{\dot{\varphi}_{-2} e V}{8 E_c^4} + \frac{\dot{\varphi}_{-1} e V}{8 E_c^3}
\end{aligned}
$$
(A46)

The term $\frac{(\dot{\varphi}_{-2})^2}{16E_c^4}$ will be added to the Lagrangian. The coupling constant for this case is,

$$\mathcal{L}_c = \frac{(\dot{\varphi}_{-1} - \dot{\varphi}_0)^2}{16E_c^1} + \frac{(\dot{\varphi}_{-1} - eV)^2}{16E_c^3} + \frac{(\dot{\varphi}_{-2})^2}{16E_c^4}, \quad (A47)$$

$$\mathcal{L} = \frac{\dot{\varphi}_+^2}{16E_c}\left(2 + \frac{NE_t}{E_g}\right) - \frac{\dot{\varphi}_+ eV}{4E_c}\left(\frac{3}{8} + \frac{E_t}{E_c}\right)$$

$$- \frac{NE_t}{16E_g E_c}\dot{\phi}eV - \frac{NE_t}{32E_g E_c}\dot{\phi}\dot{\varphi}_+ \quad (A48)$$

$$- \frac{E_t}{8E_g E_c}\sum_\mu \frac{c_\mu o_\mu}{\sqrt{2(N-1)s_\mu^2}}\dot{\xi}_\mu eV$$

$$- \frac{E_t}{8E_g E_c}\sum_\mu \frac{c_\mu o_\mu}{\sqrt{2(N-1)s_\mu^2}}\dot{\xi}_\mu\dot{\varphi}_+ + \mathcal{O}(e^2 V^2) \quad (A49)$$

$$+ \Big[(M_{00} + G_{00})\dot{\phi}^2 + 2\sum_\mu (M_{0\mu} + G_{0\mu})\dot{\phi}\dot{\xi}_\mu$$

$$+ \sum_{\mu,\nu}(M_{\mu\nu} + G_{\mu\nu})\dot{\xi}_\mu\dot{\xi}_\nu\Big] - \mathcal{U} \quad (A50)$$

a.   Hamiltonian: All terms in the Hamiltonian (H_2) can be adopted [ER: what do you mean by adopted?] via $N \rightarrow N - 1$. If $C_g^N \neq C_g^1$ then this ground fluxonium and floating fluxonium have a larger difference in terms of frequencies of modes. However, we see that by adjusting the values of the differential capacitance C and coupling capacitances C_c, we can optimize the three circuits to have the same qubit and parasitic mode frequencies. See Fig. 11 and Table V for further details.

Appendix B: Undriven Fluxonium Circuit

In this appendix, we summarize the expressions for coupling strengths and charging energies derived above and compare them for all three circuits. We will also analyze effect of variations in circuit parameters on these quantities. This analysis is used in Sec IV to comment on mitigation strategies for the parasitic effects captured in this work. We also discuss the quantities related to the corresponding dispersive qubit Hamiltonians and give expressions for the dispersive coupling $\chi_{\phi\mu}$ used in Sec. III D. Following the main text, we set $\hbar = 1$.

In Table V we note that in addition to the preserved symmetries which restrict qubit couplings to only even parasitic modes, in all three circuits, the values of parasitic quantities $g_{\phi\mu}, g_{\phi r}, \chi_{\phi\mu}$ for $\mu = 2$ are also very similar. Since the parasitic state transitions (PMIST) and the post readout parasitic-dephasing are determined predominantly by these quantities only, this observation leads to our conclusion that the various grounding configurations covered in App. A will have the same Floquet landscape. These arguments hold for all parasitic modes μ as shown by Figs. 11(d) and 15.

Fluxonium Parameters ($\mu = 2$)	Parallel Circuit H_1	Floating Fluxonium H_2	Grounded Fluxonium H_3
$g_{\phi\mu}$	157 GHz	161 GHz	158 GHz
$g_{\mu r}$	4.223 MHz	3.971 MHz	3.128 MHz
$\chi_{\phi,\mu}$	-1.1 MHz	-1.3 MHz	-1.1 MHz

TABLE V. **Parasitic quantities for the mode $\mu = 2$ across various ground configurations shown in Fig. 11(a-c).** The table gives values of coupling strengths between the qubit and the readout $g_{\phi\mu}$, readout and the parasitic-mode $g_{\phi r}$, parasitic-qubit $g_{\mu r}$ and the dispersive shift due to the parasitic mode $\chi_{\phi\mu}$.

1.   Variation in Charging energies and Coupling Strengths with Circuit Parameters

Here, we summarize the expressions for couplings and charging energies for the three circuits as derived in App. A for circuits in Figs. 11(b,c) and Ref. [26] for circuit in Figs. 11(a). We will use these expressions to show the variations with number of junctions N and parasitic ground capacitance C_g, used in Sec. IV. [SS: check these expressions after derivation. Also multiply the charge fluctuations.]
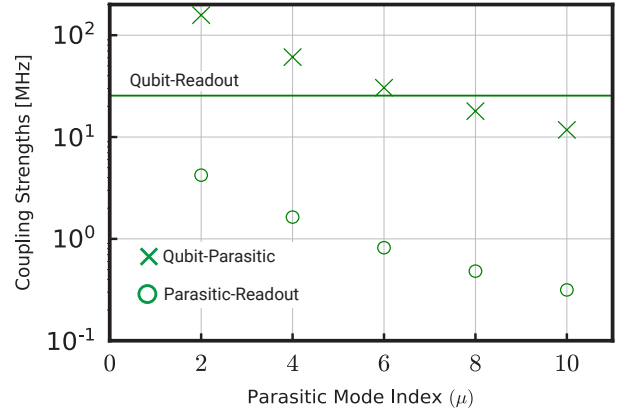

FIG. 12. **Absolute values of the coupling strengths.** $g_{\phi r}/2\pi$ (qubit-readout), $g_{\phi\mu}/2\pi$ (qubit-parasitic), $g_{\mu r}/2\pi$ (parasitic-readout), for various circuits. Coupling to odd parasitic modes is zero due to the symmetries of the circuit [26]. The parasitic modes $\mu \in \{2, 4, 6\}$ couple to the qubit more strongly than the readout.

1. Total ground capacitance.
   (a) H_1 : $E_t = \left(\frac{N-1}{E_g} + \frac{2}{E_{g1}} + \frac{2}{E_c}\right)^{-1} = 0.57$ GHz
   (b) H_2 : $E_t = \left(\frac{N-1}{E_{g,j}} + \frac{2}{E_{g_p}} + \frac{1}{E_c}\right)^{-1}$
   (c) H_3 : $E_t = \left(\frac{N-1}{E_{g,j}} + \frac{1}{E_{g_p}} + \frac{1}{E_c}\right)^{-1}$

2. Qubit Charging energy $(4E_c^\phi \hat{N}_\phi^2)$.
   (a) H_1 : $\bar{E}_c^\phi = \left(\frac{1}{4E_t}\left(1 - \frac{2}{3}\frac{(N+1)(N-1)}{N}\frac{E_t}{E_g}\right) + \frac{1}{E_{C'}} + \frac{1}{NE_{C_j}}\right)^{-1} = 0.92$ GHz.
   (b) H_2 : $\bar{E}_c^\phi = \left(\frac{1}{4E_t}\left(1 - \frac{E_t}{E_c}\right)^2\left[1 - \frac{2}{3}\frac{N-1}{N}\right] + \frac{1}{E_{C_p}} + \frac{1}{NE_{C_j}}\right)^{-1}$.

(c) H_3 : $\bar{E}_c^\phi = \left(\frac{1}{4E_t}\left(1-\frac{E_t}{E_c}\right)^2\left[1-\frac{2}{3}\frac{N-2}{N-1}\right] + \frac{1}{E_{C_p}} + \frac{1}{NE_{C_j}}\right)^{-1}$.

3. Even Parasitic Mode Charging Energy $(4E_{c,\mu}^e \hat{N}_\mu^2)$.

   (a) H_1 : $\tilde{E}_{c,\mu}^e = \left(\frac{1}{E_{C_j}} + \frac{1}{4E_g s_\mu^2}\right)^{-1}$

   (b) H_2 : Same as H_1

   (c) H_3 : Same as H_1

4. Qubit-Readout Coupling $(g_{\phi r} N_{\phi,\mathrm{ZPF}} N_{\mu,\mathrm{ZPF}})$.

   (a) H_1 : $\frac{\tilde{E}_c^\phi}{E_c}$

   (b) H_2 : $\frac{\bar{E}_c^\phi}{E_c}\left[\frac{(N+1)E_t}{2E_{g,j}} + \frac{E_t^2 \tilde{E}_{c,\mu}^o}{8E_{g,j}^2 E_c}\left(\frac{c_\mu^2}{2N s_\mu^4}\right)\right]$

   (c) H_3 : $\frac{\bar{E}_c^\phi}{E_c}\left[\frac{NE_t}{2E_{g,j}} + \frac{E_t^2 \tilde{E}_{c,\mu}^o}{8E_{g,j}^2 E_c}\left(\frac{c_\mu^2}{2(N-1)s_\mu^4}\right)\right]$

5. Qubit-Parasitic Coupling $(g_{\phi\mu} N_{\phi,\mathrm{ZPF}} N_{\mu,\mathrm{ZPF}})$

   (a) H_1 : $\sqrt{\frac{2}{N}}\frac{\tilde{E}_c^\phi \tilde{E}_{c,\mu}^e c_\mu}{E_{g,j}s_\mu^2}$

   (b) H_2 : $\sqrt{\frac{2}{N}}\frac{\bar{E}_c^\phi \tilde{E}_{c,\mu}^e c_\mu}{E_{g,j}s_\mu^2}$

   (c) H_3 : $\sqrt{\frac{2}{N-1}}\frac{\bar{E}_c^\phi \tilde{E}_{c,\mu}^e c_\mu}{E_{g,j}s_\mu^2}$

6. Readout-Parasitic Coupling $(g_{\mu r} N_{\mu,\mathrm{ZPF}} V_{\mathrm{ZPF}})$

   (a) H_1 : $\frac{\tilde{E}_c^\phi \tilde{E}_{c,\mu}^e c_\mu}{4\sqrt{2N}E_{g,j}E_c s_\mu^2}$

   (b) H_2 : $\frac{\bar{E}_c^\phi \tilde{E}_{c,\mu}^e c_\mu}{4\sqrt{2N}E_{g,j}s_\mu^2 E_c}\left[\frac{(N+1)E_t}{2E_g}\right]$

   (c) H_3 : $\frac{\bar{E}_c^\phi \tilde{E}_{c,\mu}^e c_\mu}{4\sqrt{2(N-1)}E_{g,j}s_\mu^2 E_c}\left[\frac{NE_t}{2E_{g,j}}\right]$

Zooming into Fig. 11(c), we can see in Fig. 12 that for all three circuits the lowest three even modes $\mu = 2, 4, 6$ couple to the qubit stronger than the readout. This observation is a backbone of our work; we find that because of this relatively large coupling strength, PMIST rates may be significant in a broader fluxonium-based quantum computers.

In Fig. 13, we show the dependence of charging energies and coupling constants on the number of junctions N as well as the ground capacitance C_g. We find that the charging energies increase with decrease in C_g and N. The parasitic charging energy is crucial in deciding the parasitic mode frequency ω_μ. A higher parasitic charging frequency relative to the readout frequency can lower the chances of PMIST effects. Thus, we prefer large C_g and N. The coupling strengths as shown in Fig. 7 induce all MIST effects. In particular, the parasitic-qubit coupling $g_{\phi\mu}$ is responsible for PMIST effects. The parasitic-readout coupling $g_{\mu r}$ on the other hand only increases population of the parasitic modes and is directly proportional to $g_{\phi\mu}$. We find that for low $g_{\phi\mu}$ a low C_g and high N is required. Thus, to reduce PMIST effects the best strategy is to target for low parasitic ground capacitance in the JJA and high junction count.
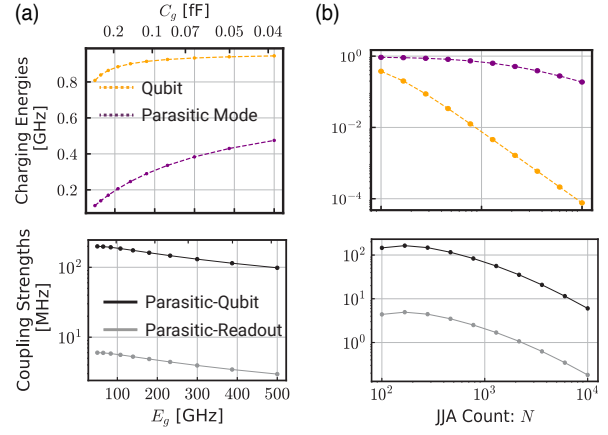

FIG. 13. **Dependence of coupling strengths and charging energies on circuit parameters.** (a) parasitic ground capacitance and (b) number of junctions in the array N. **(Top row)** The qubit charging energy decides the frequency ω_{01} and the parasitic charging energy decides the parasitic mode frequency for mode $\mu = 2$. **(Bottom row)** give the plots for the coupling strengths of the parasitic mode to readout and qubit, respectively. All plots are obtained under linear JJA approximation.

a. Variation in coupling strength. Note that, changing N changes the target inductance of the qubit. When increasing N, we need to proportionally increase the energies E_{J_j} to fix the inductive energy of the qubit ($E_L = E_{J_j}/N$). However, E_{J_j} is constrained within a typical fabrication process window, capping the maximum E_L. This further supports the large N approximation $\tilde{E}_{c,\mu}^e \approx 4E_{g,j}s_\mu^2$ (see Eq. 10). Thus, the number of junctions N can be optimized to decrease $g_{\phi\mu}$ while keeping E_L constant.

However, increasing N while keeping $E_L, E_{g,j}$ constant also decreases the parasitic charging energy (see Fig. 13 in App. B 1). For large N and small μ limit,

$$\tilde{E}_{c,\mu}^e \propto 1/N^2, \tag{B1}$$

which corresponds to lowering the parasitic mode frequency ω_μ with increasing N. This outcome is generally not favorable towards reducing PMIST, as discussed in the next section. However, in the absence of any coupling to the qubit $g_{\phi\mu}$, even a low frequency parasitic mode will be of no consequence to PMIST effects.

b. Variation in parasitic charging energy. Eqs. 11-B1 show that, for large N and small μ limit, ω_μ^e is inversely proportional to N^2 and $C_{g,j}$ [fF] $= \frac{19.4}{E_{g,j}\,[\mathrm{GHz}]}$ (see Fig. 13 in App. B 1). Thus, again, a smaller parasitic ground capacitance $C_{g,j}$ increases the parasitic mode charging energy, thus increasing its frequency, favorably. However, in contrast with the case of coupling strength $g_{\phi\mu}$, a larger N leads to lower frequencies for these modes, which is unfavorable since it decreases the gap between the between ω_d and ω_μ. We already discussed the complications of changing the ground capacitance $C_{g,j}$ in the previous discussion of coupling strengths above. The impact of decreasing N would require careful consideration of increased nonlinearity of

the parasitic modes as well as increased coupling strengths.

2. Fluxonium Qubit Hamiltonian

[SS: check for units to be $\hbar = 1$] We now discuss the Fluxonium qubit Hamiltonian, through a detailed consideration of its charge matrix elements and the dispersive shifts on the qubit induced by the parasitic modes and readout. This dispersive Hamiltonian is derived using the Schrieffer-Wolff approximation [26]. The qubit Hamiltonian H_ϕ (see Eq. 2) is diagonalized in the Fock state basis, where we have used the standard bosonic operators

$$\hat{x} = x_{\text{ZPF}}(a + a^\dagger) = \hat{N}_\phi / N_{\phi,\text{ZPF}} \qquad (B2)$$

and

$$\hat{p} = -ip_{\text{ZPF}}(a - a^\dagger) = \hat{\phi}/\phi_{\text{ZPF}}. \qquad (B3)$$

such that $[\hat{x}, \hat{p}] = i$.

a. Charge Matrix Elements for H_1, H_2, H_3: Here, using the approximations described in App. A, we calculate the charge matrix elements for the qubit mode. We observe that with increasing final state (f), the charge matrix elements with respect to the ground and first two excited states follow a decreasing trend, approximately exponential. This exponential decrease to 10^{-10} motivates our truncation of the fluxonium potential up to 30 levels for the Floquet simulations of Sec. III.
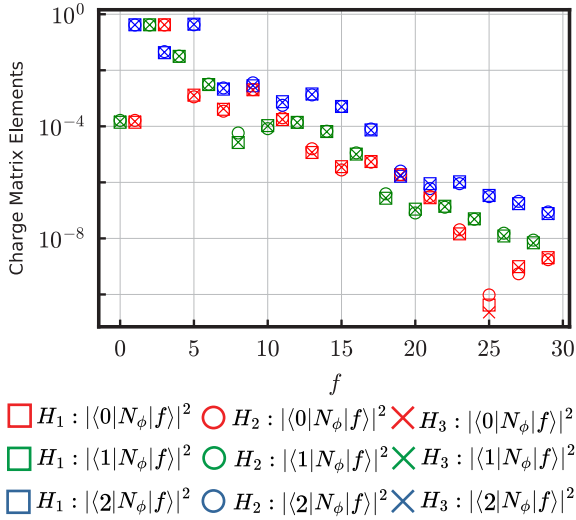

FIG. 14. **Charge matrix elements (squared) for all three circuits.** Note that we use $\langle f|N_\phi|f'\rangle = iN_{\phi,\text{ZPF}}\langle f|(a - a^\dagger)|f'\rangle$ where $N_{\phi,\text{ZPF}} = \frac{1}{\sqrt{2}}\left(E_{J,j}/8NE_c\right)^{1/4}$. The charge matrix elements between parity conserving states is zero (points not seen in log plot) due to the symmetry of cosine potential at $\varphi_{\text{ext}} = 0.5\Phi_0$, where Φ_0 is the flux quantum.

b. Dispersive Hamiltonian Next, we extract the qubit parameters quoted in Table II, for example, the dispersive shift of the qubit due to the parasitic modes

$\chi_{\phi\mu}$ and the readout mode $\chi_{\phi r}$ [26]. These variables were used to generate Fig. 6 in the main text. For this purpose, we first give the qubit Hamiltonian in the dispersive regime [26],

$$H/\hbar = \frac{\omega_q}{2}\sigma_z + \sum_\mu(\omega_\mu + k_\mu)a_\mu^\dagger a_\mu + \omega_r a_r^\dagger a_r$$
$$+ \chi_{r,\phi}\sigma_z a_r^\dagger a_r + \sum_\mu \chi_{\mu,\phi}\sigma_z a_\mu^\dagger a_\mu$$
$$+ \sum_\mu \chi_{r\mu}a_\mu^\dagger a_\mu a_r^\dagger a_r \qquad (B4)$$
$$= \frac{\omega_q}{2}\sigma_z + \left(\omega_r + \chi_{r\phi}\sigma_z\right)a_r^\dagger a_r$$
$$+ \sum_\mu \left(\omega_\mu + k_\mu + \chi_{r\mu}a_r^\dagger a_r + \chi_{\mu\phi}\sigma_z\right)a_\mu^\dagger a_\mu \quad (B5)$$

where the lamb shift is given by,

$$k_{\mu\in 2\mathbb{Z}} = 16E_{C_r}^2\sqrt{\frac{E_{L_r}}{32E_{C_r}}}\sqrt{\frac{E_{J_j}}{32E_c^e}}\left[\frac{g_{r\mu}^2}{\omega_\mu - \omega_r}\right] \quad (B6)$$

$\leq \mathcal{O}(10^{-8})$. In Eq. B5 the qubit frequency is given by $\omega_{01} = \epsilon_1 - \epsilon_0$

$$= -|\langle 0|p_\phi|1\rangle|^2\left[16g_{r\phi}^2E_{C_r}^2\sqrt{\frac{E_{L_r}}{32E_{C_r}}}\frac{2\epsilon_{01}}{\epsilon_{01}^2 - \omega_r^2}\right.$$
$$+ \sum_\mu\left\{g_{\mu\phi}^2\sqrt{\frac{E_{J_j}}{32\tilde{E}_{C,\mu}^e}}\frac{2\epsilon_{01}}{\epsilon_{01}^2 - \omega_\mu^2}\right\}\right]$$
$$- \sum_{l>1}16g_{r\phi}^2E_{C_r}^2\sqrt{\frac{E_{L_r}}{32E_{C_r}}}\left[\frac{|\langle 0|p_\phi|l\rangle|^2}{\epsilon_{0l} - \omega_r}\right.$$
$$\left. - \frac{|\langle 1|p_\phi|l\rangle|^2}{\epsilon_{1l} - \omega_r}\right] + \sum_{l>1,\mu}\left\{g_{\mu\phi}^2\sqrt{\frac{E_{J_j}}{32\tilde{E}_{C,\mu}^e}}\times\right.$$
$$\left.\left[\frac{|\langle 0|p_\phi|l\rangle|^2}{\epsilon_{0l} - \omega_\mu} - \frac{|\langle 1|p_\phi|l\rangle|^2}{\epsilon_{1l} - \omega_\mu}\right]\right\} \quad (B7)$$

Here the second summand over μ is the correction $\delta_{\omega_{01}}$ to the qubit frequency due to parasitic modes. For the parameters used in Table I, which yields $\omega_{01}/2\pi = 30$ MHz the frequency corrections for circuits H_1, H_2, H_3 are $\delta\omega_{01}/2\pi = 0.4$ MHz, 0.45 MHz, 0.41 MHz, respectively.

The dispersive shift due to the readout mode is given by,

$$\chi_{\phi r} = 16g_{r\phi}^2E_{C_r}^2\sqrt{\frac{E_{L_r}}{32E_{C_r}}}\frac{2\epsilon_{01}}{\epsilon_{01}^2 - \omega_r^2}|\langle 0|p_\phi|1\rangle|^2$$
$$+ 16g_{r\phi}^2E_{C_r}^2\sqrt{\frac{E_{L_r}}{32E_{C_r}}}\left[\sum_l|\langle 0|p_\phi|l\rangle|^2\frac{\epsilon_{0l}}{\epsilon_{0l}^2 - \omega_r^2}\right.$$
$$\left. - \sum_l|\langle 1|p_\phi|l\rangle|^2\frac{\epsilon_{1l}}{\epsilon_{1l}^2 - \omega_r^2}\right] \quad (B8)$$

and the dispersive shift due to the parasitic mode is given by,

$$\chi_{\phi\mu} = g_{\mu\phi}^2\sqrt{\frac{E_{J_j}}{32\tilde{E}_{C,\mu}^e}}\frac{2\epsilon_{01}}{\epsilon_{01}^2 - \omega_\mu^2}|\langle 0|p_\phi|1\rangle|^2$$

$$+ g_{\mu\phi}^2 \sqrt{\frac{E_{J_j}}{32\tilde{E}_{C,\mu}^e}} \left[\sum_l |\langle 0|p_\phi|l\rangle|^2 \frac{\epsilon_{0l}}{\epsilon_{0l}^2 - \omega_\mu^2} \right.$$
$$\left. - \sum_l |\langle 1|p_\phi|l\rangle|^2 \frac{\epsilon_{1l}}{\epsilon_{1l}^2 - \omega_\mu^2} \right] \tag{B9}$$

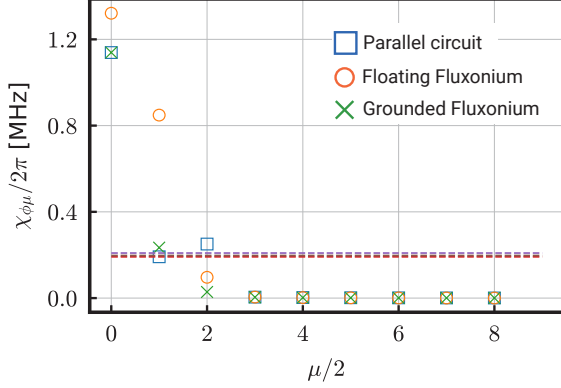For the parameters in Table I, we plot $\chi_{\phi\mu}, \chi_{\phi r}$ for all three circuits in Fig. 15.

FIG. 15. **The dispersive shift induced on the qubit due to the parasitic mode μ.** The three grounding configurations, parallel circuit (H_1), floating fluxonium (H_2), and grounded fluxonium (H_3) shown in Figs. 13(a-c) yield the same values. Dashed lines in the same color code represent the dispersive shift ($\sim$) induced by the readout resonator on the qubit.

Appendix C: Driven Fluxonium Circuit

Here, we discuss the several analysis techniques to study MIST effects used in this work. We begin with the derivation of $H_{s.c.}$ in Eq. 6. Then we discuss and justify the Hilbert space truncation, as well as approximations used for Floquet simulations in Sec. III.

1. Semi-classical Approximation

[SS: include the derivation]

2. Approximations for Numerical Modeling

We use the following three approximations in our work.

- **Restriction to $\mu = 2$.** We restrict our analyses to only include the lowest-frequency, even parasitic mode. This mode couples most strongly to the qubit and the readout as evident from Fig. 12(d). This assumption reduces the Hilbert space size for feasible study.

- **Semi-classical drive approximation.** We treat the readout resonator classically as described in Refs. [20–23], eliminating the readout mode states from our numerical simulation. This approximation is again necessary to restrict

the Hilbert space size to values feasible for numeric study.

- **Linear JJA Approximation.** We assume that the parasitic modes are linear, due to the large $E_{J_j}/E_{C_j} \sim 200$ ratio. Nonlinear corrections to our results is beyond the scope of this work. For details on how nonlinear corrections affect different circuit energies, we direct the readers to Ref. [26].

- **Truncation.** We note that the charge matrix elements connecting the fluxonium qubit ground states to excited states decreases roughly exponentially with increasing excited state number. With this observation, shown in Fig. 14, as well as our assumptions above, we truncate the Hilbert space dimensions to $30 \otimes 10$. That is, we assume 30 levels in the fluxonium qubit mode and 10 levels in the parasitic mode.

Note that for the conclusions drawn in this paper, we are only interested in identifying the existence of PMIST processes, and do not claim to quantify how many such transitions can be present. Hence, with this truncation we only examine the excitations to $0-2$ levels in the parasitic mode and $0-20$ in the fluxonium subspace in Figs. 3, 9, 7. In this appendix we will show the results for truncating the Hilbert space to $20 times 5$ levels in the two modes and $30 times 10$, showing the convergence of the MIST results.

[SS: Include the 30 X 10 as well as 20 X 3]

3. Floquet Simulations

a. Stark shift: To observe a state transition the primary requirements are high charge matrix elements and low energy difference. The eigen-energies of the states in question are changed with an increase in the number of readout photons or, in this case, the drive strength. In this section, we compute the Stark shifted eigen-energies which facilitates the prediction of an avoided crossing using a first-order perturbative approach, given $\bar{n}_r, \omega_r$ and the charge matrix elements. Let $|i\rangle$ be a state in the eigenspace of $H_{int} = H_\phi + H_{\mu=2} + g_{\phi\mu}\hat{N}_\phi\hat{N}_\mu$. Following derivations in App. B, the Stark-shift in the energy of state $|i\rangle$ at an average number of readout photons $\bar{n}_r$ is given by

$$\chi_i(\bar{n}_r) = 2\bar{n}_r \sum_f \omega_{if} \left[\frac{g_{\phi r} |\langle i|\hat{N}_\phi|f\rangle|^2}{\omega_d^2 - \omega_{if}^2} + \frac{g_{\mu r} |\langle i|\hat{N}_\mu|f\rangle|^2}{\omega_d^2 - \omega_{if}^2} \right] \tag{C1}$$

Here $\omega_{if} = E_f - E_i$ denote the energy difference in the eigen-energies of the state $|i\rangle$. The impact due to the second term is much smaller than the first term, and hence $g_{\phi r}$ primarily governs this Stark shift.

b. Population exchange and quasienergies: Below we plot the population exchange and quasienergy probabilities for all transitions captured in Fig. 3 and Table III for states $|\tilde{0}, \tilde{0}\rangle$ (see Fig. 20), $|\tilde{1}, \tilde{0}\rangle$ (see Fig. 21) and $|\tilde{2}, \tilde{0}\rangle$ (see Fig. 22). We will comment on some special types of transitions explicitly here.
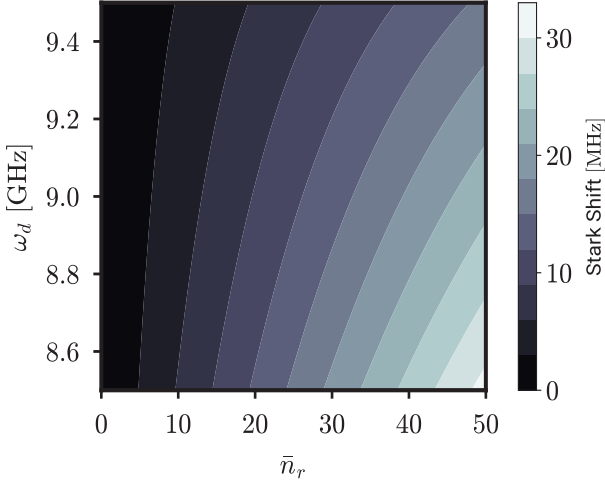
FIG. 16. Stark shift in different energy levels for readout computed using Eq. C1 for energy level $|\tilde{0}, \tilde{0}\rangle$. We have verified that Stark shift on the excited energy levels $|\tilde{1}, \tilde{0}\rangle$ and $|\tilde{2}, \tilde{0}\rangle$ are also upper bounded by 50 MHz for the ranges considered in x- and y-axes in this plot.

- Transition (2) has two crossings, one that takes place at $\bar{n}_r = 14$ and another at $\bar{n}_r = 48$. The states $|\tilde{4}, \tilde{2}\rangle$ and $|\tilde{14}, \tilde{2}\rangle$ hybridize first and then the resulting state hybridizes with the computational state $|\tilde{0}, \tilde{0}\rangle$.

- Transitions $(3, 4)$ show a branch bunching scenario, as quoted in Ref. [23] for the case of positive detuning. However, in this case we note that both branch bunching and crossings were observed in the negative detuning case. Such branch bunching occurs when the drive frequency (ω_d) is equal to the transition frequency of two states $i, j(\omega_{ij})$. In the presence of parasitic mode, there are multiple states ($|\tilde{i}, \tilde{\mu}\rangle$ and $|\tilde{j}, \tilde{\mu}\rangle$ for various μ) such that $\omega_d = \omega_{ij}$ is the resonant frequency for the observation of bunching between the two states.

- In transitions $(9, 11, 12)$ the states do not return to the same population as the initial states. This is the case because we are plotting the bare fluxonium and parasitic mode operators $\langle \bar{n}_\phi \rangle, \langle \bar{n}_\mu \rangle$. We make this choice to show the impact of PMIST effects on the bare fluxonium population since the parasitic modes have been ignored in most previous fluxonium analyses.

- Finally, in transition (14) we again see two crossings. In the absence of qubit-parasitic coupling $g_{\phi\mu}$ this transition is only carried out between $|\tilde{17}, \tilde{0}\rangle$ and $|\tilde{2}, \tilde{0}\rangle$. However, in the presence of parasitic modes $|\tilde{17}, \tilde{0}\rangle$ hybridizes with $|\tilde{5}, \tilde{1}\rangle$ which then has a branch crossing with $|\tilde{2}, \tilde{0}\rangle$. Thus, in this case we see that ignoring parasitic modes can lead to wrong state predictions which could affect the qubit reset post measurement.

c. Landau-Zener probabilities: We compute the Landau-Zener probabilities in Sec. III C numerically

using the quasienergies from the Floquet simulations, and analytically, using the Stark-shifted eigenenergies. In this case, we use a time-dependent readout photon number, where $\bar{n}_r$ varies as $\bar{n}_r = 50(1 - e^{-\kappa t/2})^2$, to emulate change in readout photons from dissipation [21?]. The numerical calculations use the probability for Landau-Zener transitions given in [31], for an avoided crossing observed between states $|i\rangle, |f\rangle$ of

$$P_{LZ} = \exp\left[- \frac{\pi \Delta_{ac}^2}{2v} \right], \quad \text{(C2)}$$

$$\text{where } v = \sqrt{2\Delta_{ac} \left| \frac{d^2 \epsilon_f}{d\sqrt{\bar{n}_r(t)}^2} \right|_{t_{ac}} \frac{d\sqrt{\bar{n}_r(t)}}{dt} |_{t_{ac}}} \quad \text{(C3)}$$

Here, the variable ϵ_j is the numerically-computed quasi-energy obtained from Floquet simulations, while Δ_{ac} refers to their quasi-energy difference at avoided crossing.

Appendix D: Alternative Circuit

Here, we give the circuit parameters (Table VI), coupling strengths (Fig. 17), charge matrix elements (Fig. 18) and state transition quasienergies shown in Figs. 10 and Fig. 19.

N	φ_{ext}	E_{J_p}	E_{C_p}	E_C	E_{C_j}	E_{J_j}	$E_{C_{g,j}}$	$E_{C_{g,p}}$	E_c
102	$0.5\Phi_0$	6.20	1.24	4.28	0.74	81.6	194	1.94	19.40

TABLE VI. Circuit parameters for Fig. 10(a) inspired by Ref. [6]. All energies are given in GHz. Here $\Phi_0 = h/2e$ denotes the magnetic flux quantum. The capacitive energies $E_{C'} = \frac{19.4}{C'(fF)}$ GHz are computed from the corresponding capacitances C'.

The coupling strengths in this circuit are similar to those evaluated for our original circuit parameters, in Fig. 12.
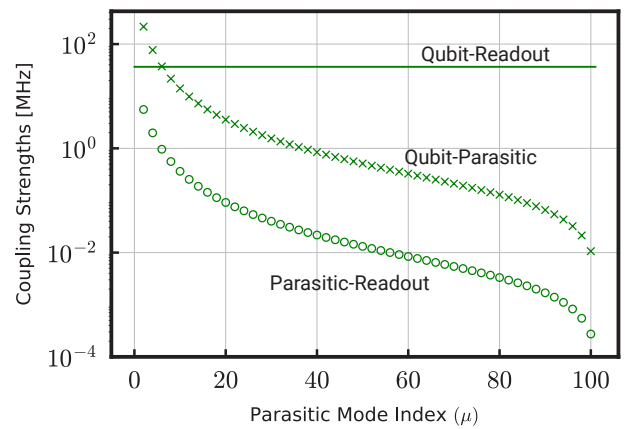

FIG. 17. **Absolute values of the coupling strengths.** $g_{\phi r}/2\pi$ (qubit-readout), $g_{\phi\mu}/2\pi$ (qubit-parasitic), $g_{\mu r}/2\pi$ (parasitic-readout), for various circuits. Coupling to odd parasitic modes is zero due to the symmetries of the circuit [26]. The parasitic modes $\mu \in \{2, 4, 6\}$ couple to the qubit more or as strongly as the readout.

We find in Fig. 18 that the charge matrix elements of the second circuit analyzed in Sec. IV C has a faster decrease with increasing excited state levels. This could be indicative of the fact that such a circuit will see lower MIST effects as observed in Fig. 10(c).
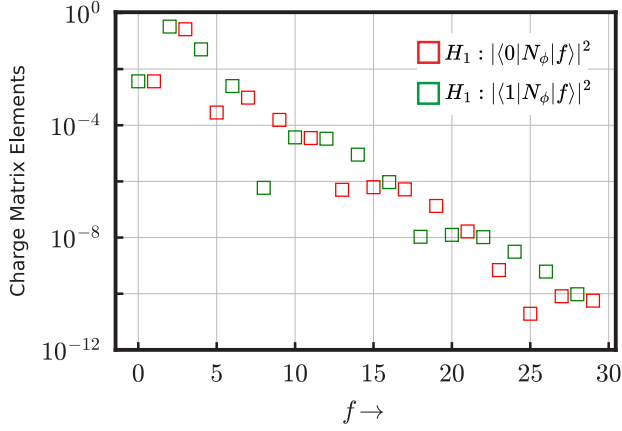

FIG. 18. **Charge Matrix Elements (squared) for all three circuits.** Note that in the equations below we substitute $\langle i|N_\phi|f\rangle = iN_{\phi,\mathrm{ZPF}}\langle i|(a - a^\dagger)|f\rangle$ where $N_{\phi,\mathrm{ZPF}} = \frac{1}{\sqrt{2}}\left(E_{J,j}/8NE_{\mathrm{C}}\right)^{1/4}$. The charge matrix elements between odd-odd or even-even is zero (points not seen in log plot) due to the symmetry of cosine potential at $\varphi_{\mathrm{ext}} = 0.5\Phi_0$, where Φ_0 is the flux quantum. Here H_1 denotes the parallel circuit in Fig. 11(a).

Finally, we plot the PMIST effect observed in the Floquet simulations for this alternative circuit in Fig. 19. We perform a branch analysis of the initial state $|\tilde{0},\tilde{0}\rangle$ and observe a transition to $|\tilde{4},\tilde{1}\rangle$, as described in the main text.
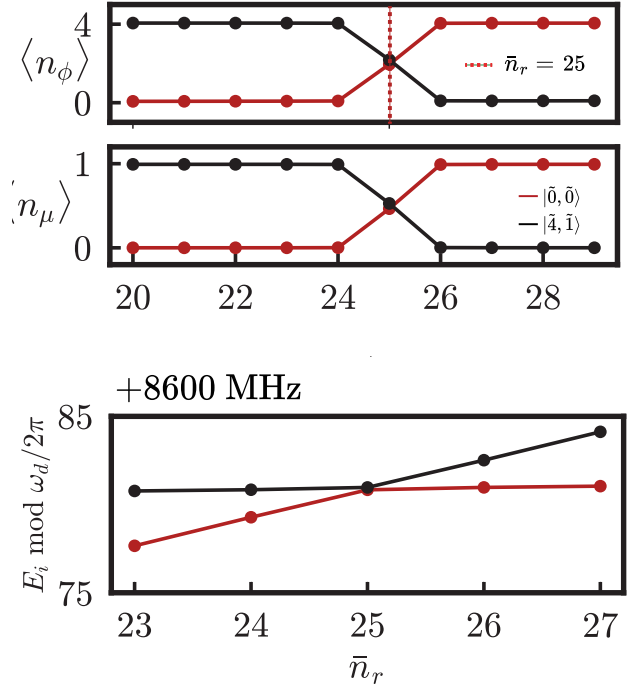

FIG. 19. **Examples of PMIST using transitions for the alternative circuit in Fig. 10(c) of Sec. IV C.** involving the states $|\tilde{0},\tilde{0}\rangle \leftrightarrow |\tilde{4},\tilde{1}\rangle$, with maximum overlap to the un-hybridized state $|k\rangle_\phi \otimes |n\rangle_{\mu=2}$. **Top row:** Qubit mode average occupation $\langle n_\phi\rangle$. **Middle row:** Parasitic mode average occupation $\langle n_\mu\rangle$. **Bottom row:** Quasi-energies (solid) from Floquet simulations showing avoided crossings. Plots are extracted from numerical data used in Fig. 3. The data points are connected by lines for visual aid.
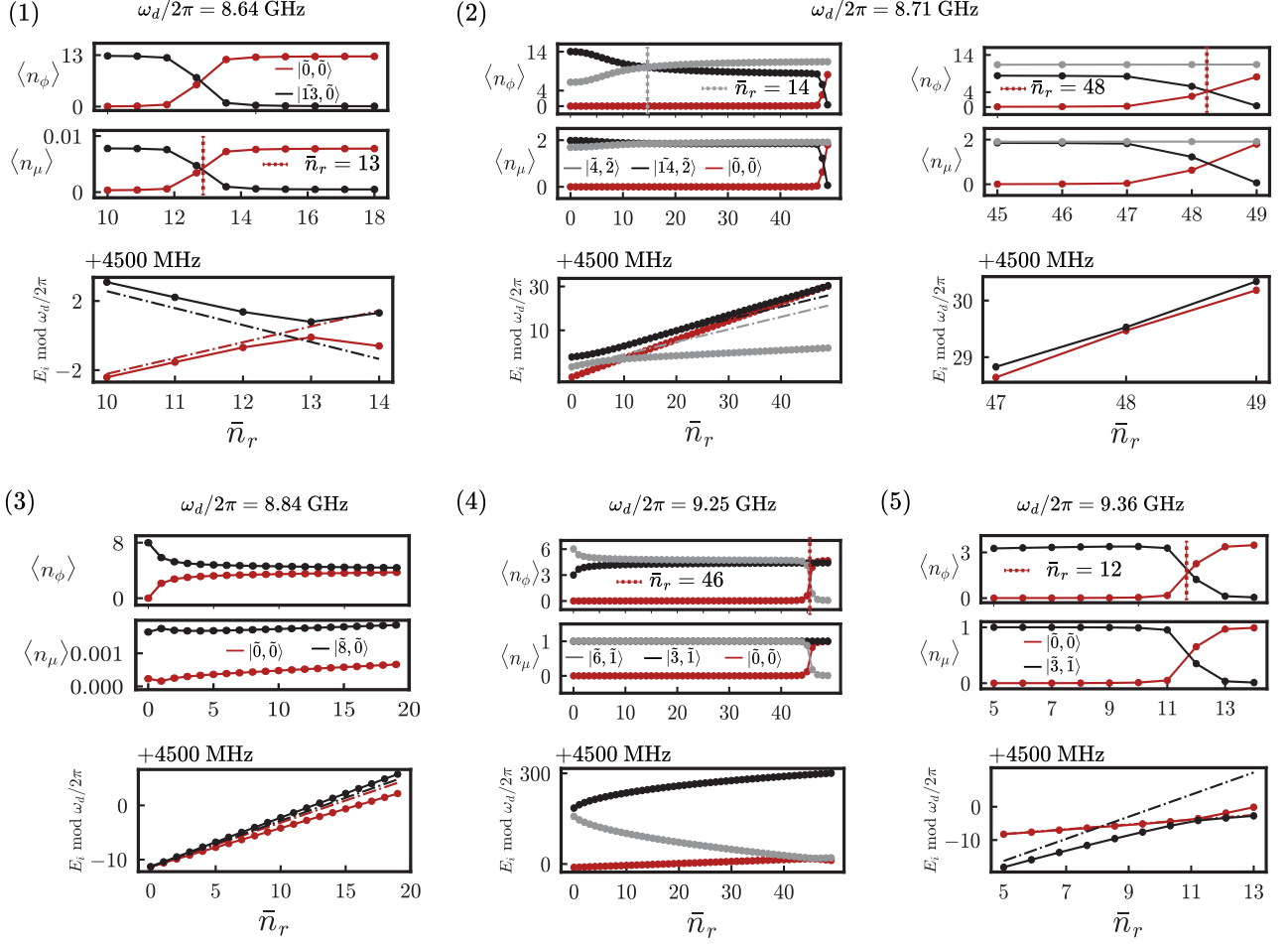
FIG. 20. MIST processes from Table III involving the $|\tilde{0}, \tilde{0}\rangle$ state in rows indexed by figure numbering. (Top row) Fluxonium subspace $\langle n_\phi \rangle$. (Middle) Parasitic mode subspace $\langle n_\mu \rangle$ (Bottom) Stark-shifted eigen-energies (dashed) and quasi-energies (solid) from Floquet simulations, corresponding to the initial state i as per the legend. The y-axis for this plot is in MHz. Floquet results are extracted from numerical data used for Fig. 3. Note that MIST in figure (2) is split into two figures in order to capture the two consecutive transitions involved.
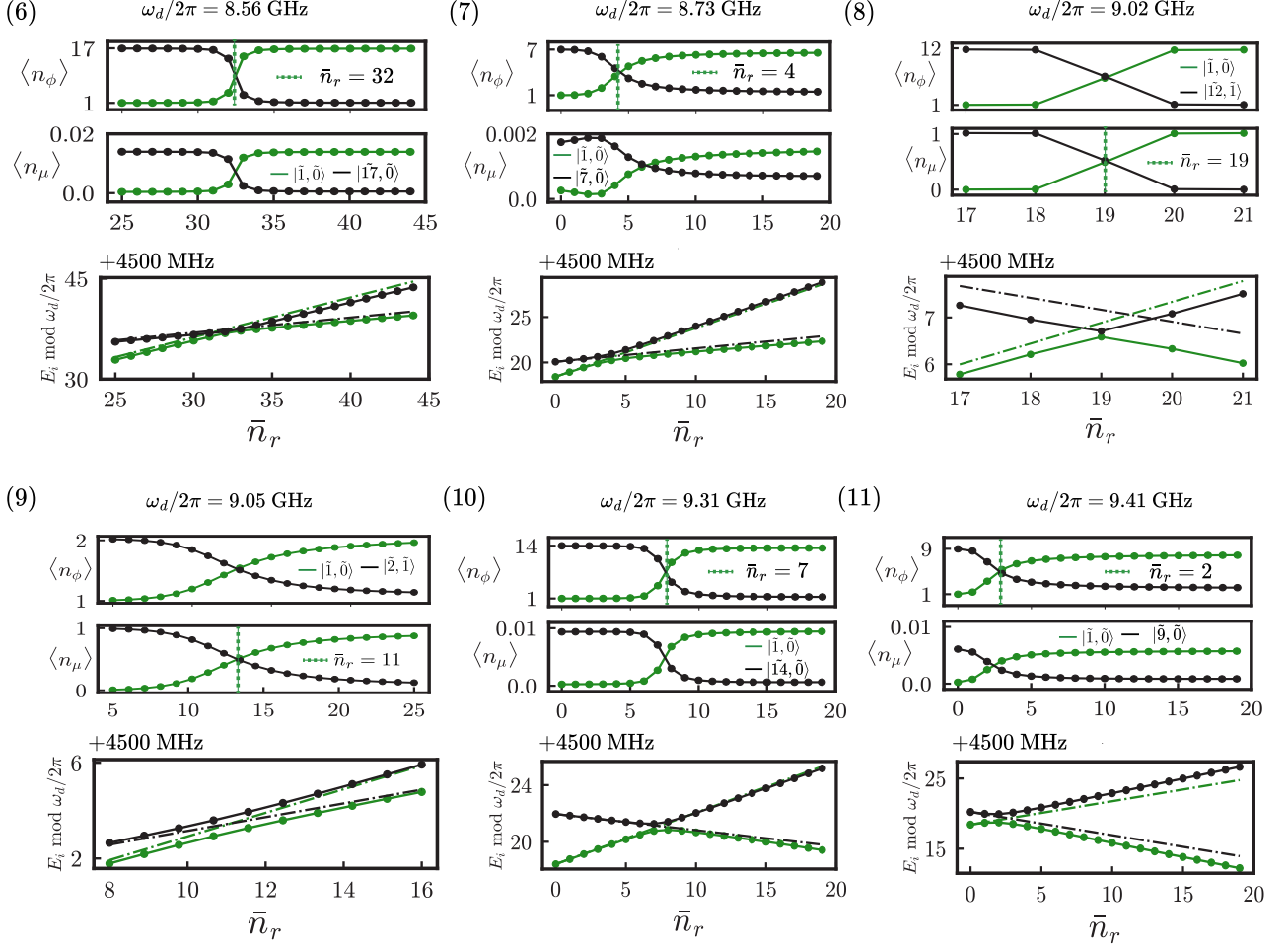
FIG. 21. MIST processes from Table III involving the $|\tilde{1}, \tilde{0}\rangle$ state in rows indexed by figure numbering. (Top row) Fluxonium subspace $\langle n_\phi \rangle$. (Middle) Parasitic mode subspace $\langle n_\mu \rangle$ (Bottom) Stark-shifted eigen-energies (dashed) and quasi-energies (solid) from Floquet simulations, corresponding to the initial state i as per the legend. The y-axis for this plot is in MHz. Floquet results are extracted from numerical data used for Fig. 3.
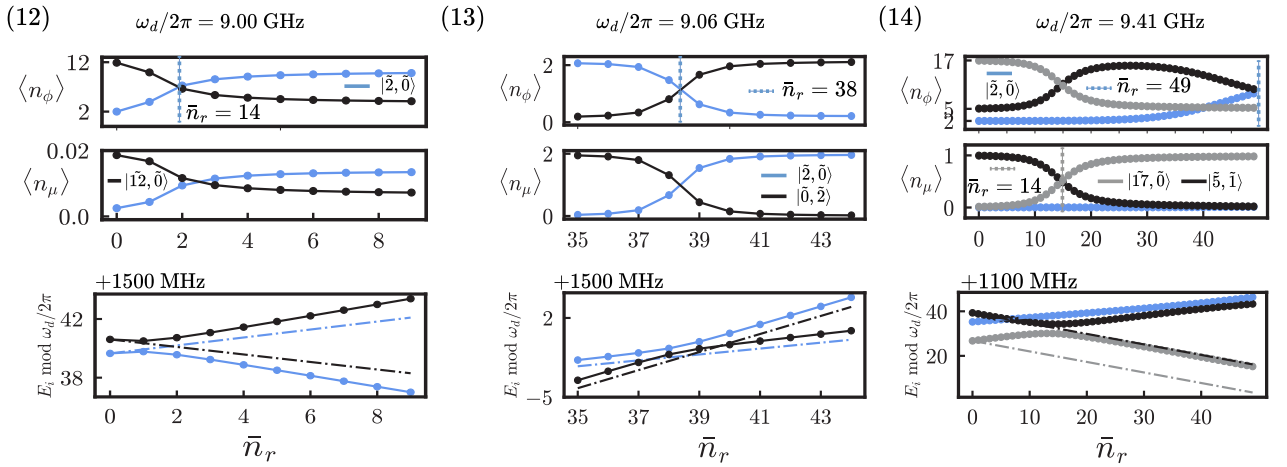

FIG. 22. MIST processes from Table III involving the $|\tilde{2}, \tilde{0}\rangle$ state in rows indexed by figure numbering. (Top row) Fluxonium subspace $\langle n_\phi \rangle$. (Middle) Parasitic mode subspace $\langle n_\mu \rangle$ (Bottom) Stark-shifted eigen-energies (dashed) and quasi-energies (solid) from Floquet simulations, corresponding to the initial state i as per the legend. The y-axis for this plot is in MHz. Floquet results are extracted from numerical data used for Fig. 3.

- Units of g is an outstanding issue: momentum or charge coefficient?

- PMIST or PIST

- some sub-figures have subheadings some do not

- shorter conclusion

[1] Phys. Rev. X 9, 041041 (2019) - High-Coherence Fluxonium Qubit (2019).

[2] A. Somoroff, Q. Ficheux, R. A. Mencia, H. Xiong, R. Kuzmin, and V. E. Manucharyan, Millisecond Coherence in a Superconducting Qubit, Physical Review Letters 130, 267001 (2023), publisher: American Physical Society.

[3] Fluxonium: Single Cooper-Pair Circuit Free of Charge Offsets | Science (2009).

[4] N. Earnest, S. Chakram, Y. Lu, N. Irons, R. K. Naik, N. Leung, L. Ocola, D. A. Czaplewski, B. Baker, J. Lawrence, J. Koch, and D. I. Schuster, Realization of a Λ system with metastable states of a capacitively shunted fluxonium, Phys. Rev. Lett. 120, 150504 (2018).

[5] H. Zhang, S. Chakram, T. Roy, N. Earnest, Y. Lu, Z. Huang, D. Weiss, J. Koch, and D. I. Schuster, Universal fast flux control of a coherent, low-frequency qubit, Physical Review X 11, 011010 (2021), arXiv:2002.10653 [cond-mat, physics:quant-ph].

[6] L. Ding, M. Hays, Y. Sung, B. Kannan, J. An, A. Di Paolo, A. H. Karamlou, T. M. Hazard, K. Azar, D. K. Kim, B. M. Niedzielski, A. Melville, M. E. Schwartz, J. L. Yoder, T. P. Orlando, S. Gustavsson, J. A. Grover, K. Serniak, and W. D. Oliver, High-Fidelity, Frequency-Flexible Two-Qubit Fluxonium Gates with a Transmon Coupler, Physical Review X 13, 031035 (2023), publisher: American Physical Society.

[7] H. Zhang, C. Ding, D. Weiss, Z. Huang, Y. Ma, C. Guinn, S. Sussman, S. P. Chitta, D. Chen, A. A. Houck, J. Koch, and D. I. Schuster, Tunable Inductive Coupler for High-Fidelity Gates Between Fluxonium Qubits, PRX Quantum 5, 020326 (2024), publisher: American Physical Society.

[8] K. N. Nesterov, C. Wang, V. E. Manucharyan, and M. G. Vavilov, cnot Gates for Fluxonium Qubits via Selective Darkening of Transitions, Physical Review Applied 18, 034063 (2022), publisher: American Physical Society.

[9] K. N. Nesterov, Q. Ficheux, V. E. Manucharyan, and M. G. Vavilov, Proposal for Entangling Gates on Fluxonium Qubits via a Two-Photon Transition, PRX Quantum 2, 020345 (2021), publisher: American Physical Society.

[10] E. Dogan, D. Rosenstock, L. Le Guevel, H. Xiong, R. A. Mencia, A. Somoroff, K. N. Nesterov, M. G. Vavilov, V. E. Manucharyan, and C. Wang, Two-Fluxonium Cross-Resonance Gate, Physical Review Applied 20, 024011 (2023), publisher: American Physical Society.

[11] E. L. Rosenfeld, C. T. Hann, D. I. Schuster, M. H. Matheny, and A. A. Clerk, Designing high-fidelity two-qubit gates between fluxonium qubits, arXiv preprint arXiv:2403.07242 (2024).

[12] PRX Quantum 3, 037001 (2022) - Blueprint for a High-Performance Fluxonium Quantum Processor (2022).

[13] N. A. Masluk, I. M. Pop, A. Kamal, Z. K. Minev, and M. H. Devoret, Microwave Characterization of Josephson Junction Arrays: Implementing a Low Loss Superinductance, Physical Review Letters 109, 137002 (2012), publisher: American Physical Society.

[14] F. Wang, K. Lu, H. Zhan, L. Ma, F. Wu, H. Sun, H. Deng, Y. Bai, F. Bao, X. Chang, et al., Achieving millisecond coherence fluxonium through overlap josephson junctions, arXiv preprint arXiv:2405.05481 (2024).

[15] A. Blais, A. L. Grimsmo, S. M. Girvin, and A. Wallraff, Circuit quantum electrodynamics, Reviews of Modern Physics 93, 025005 (2021).

[16] D. Gusenkova, M. Spiecker, R. Gebauer, M. Willsch, D. Willsch, F. Valenti, N. Karcher, L. Grünhaupt, I. Takmakov, P. Winkel, et al., Quantum nondemolition dispersive readout of a superconducting artificial atom using large photon numbers, Physical Review Applied 15, 064030 (2021).

[17] U. Vool, A. Kou, W. C. Smith, N. E. Frattini, K. Serniak, P. Reinhold, I. M. Pop, S. Shankar, L. Frunzio, S. M. Girvin, and M. H. Devoret, Driving forbidden transitions in the fluxonium artificial atom, Phys. Rev. Appl. 9, 054046 (2018).

[18] U. Vool, I. M. Pop, K. Sliwa, B. Abdo, C. Wang, T. Brecht, Y. Y. Gao, S. Shankar, M. Hatridge, G. Catelani, M. Mirrahimi, L. Frunzio, R. J. Schoelkopf, L. I. Glazman, and M. H. Devoret, Non-poissonian quantum jumps of a fluxonium qubit due to quasiparticle excitations, Phys. Rev. Lett. 113, 247001 (2014).

[19] R. Shillito, A. Petrescu, J. Cohen, J. Beall, M. Hauru, M. Ganahl, A. G. Lewis, G. Vidal, and A. Blais, Dynamics of transmon ionization, Physical Review Applied 18, 034031 (2022).

[20] X. Xiao, J. Venkatraman, R. G. Cortiñas, S. Chowdhury, and M. H. Devoret, A diagrammatic method to compute the effective hamiltonian of driven nonlinear oscillators, arXiv preprint arXiv:2304.13656 (2023).

[21] M. Khezri, A. Opremcak, Z. Chen, K. C. Miao, M. McEwen, A. Bengtsson, T. White, O. Naaman, D. Sank, A. N. Korotkov, et al., Measurement-induced state transitions in a superconducting qubit: Within the rotating-wave approximation, Physical Review Applied 20, 054008 (2023).

[22] J. Cohen, A. Petrescu, R. Shillito, and A. Blais, Reminiscence of classical chaos in driven transmons, PRX Quantum 4, 020312 (2023).

[23] M. F. Dumas, B. Groleau-Paré, A. McDonald, M. H. Muñoz Arias, C. Lledó, B. D'Anjou, and A. Blais, Measurement-induced transmon ionization, Phys. Rev. X 14, 041023 (2024).

[24] D. Sank, Z. Chen, M. Khezri, J. Kelly, R. Barends, B. Campbell, Y. Chen, B. Chiaro, A. Dunsworth, A. Fowler, et al., Measurement-induced state transitions in a superconducting qubit: Beyond the rotating wave approximation, Physical review letters 117, 190503 (2016).

[25] K. N. Nesterov and I. V. Pechenezhskiy, Measurement-induced state transitions in dispersive qubit readout schemes, arXiv preprint arXiv:2402.07360 (2024).

[26] G. Viola and G. Catelani, Collective modes in the fluxonium qubit, Physical Review B 92, 224511 (2015).

[27] V. E. Manucharyan, J. Koch, L. I. Glazman, and M. H. Devoret, Fluxonium: Single cooper-pair circuit free of charge offsets, Science 326, 113 (2009).

[28] Note that the ground capacitances C_{g_n} are distinct from the self-capacitance $\frac{19.4}{E_{C,j}(\text{GHz})}$ fF (see Table IV) across the junctions in the array, which set the junction array plasmon frequency [39].

[29] D. G. Ferguson, A. A. Houck, and J. Koch, Symme-

tries and collective excitations in large superconducting circuits, Physical Review X **3**, 011003 (2013).

[30] In fact, the first four even parasitic modes with coupling strengths within a factor of 10 of $g_{\phi r}$. See Fig. 12 in App. B 1.

[31] T. N. Ikeda, S. Tanaka, and Y. Kayanuma, Floquet-landau-zener interferometry: Usefulness of the floquet theory in pulse-laser-driven systems, Physical Review Research **4**, 033075 (2022).

[32] We show that our results hold when simulated with 30 levels in the qubit mode and 10 levels in the parasitic mode.

[33] A relatively high-frequency choice, to reduce thermal, photon shot-noise induced dephasing in the qubit compared to lower-frequency bands.

[34] G. Zhu, D. G. Ferguson, V. E. Manucharyan, and J. Koch, Circuit QED with fluxonium qubits: Theory of the dispersive regime, Physical Review B **87**, 024510 (2013), publisher: American Physical Society.

[35] N. A. Masluk, *Reducing the losses of the fluxonium artificial atom* (Yale University, 2013).

[36] A. G. Fowler, M. Mariantoni, J. M. Martinis, and A. N. Cleland, Surface codes: Towards practical large-scale quantum computation, Physical Review

A—Atomic, Molecular, and Optical Physics **86**, 032324 (2012).

[37] Further lower ω_{d} for readout is not favorable due to thermal heating of the readout resonator leading to photon-shot-noise induced dephasing of the qubit, and hence not analyzed in this work.

[38] If $\omega_{\mathrm{d}} \gg \omega_{\mu=N-1}$, a dominating transition mechanism for PMIST would correspond to an excitation of a strongly coupled, low-frequency parasitic mode (i.e., $\mu = \{2, 4, 6\}$) to a large photon number y, leaving just enough energy to produce excitation to some state f in the fluxonium subspace of significant charge matrix elements (see Fig. 14). However such large excitations in the parasitic modes would occur with lower probability, because of the high photon number y involved in the transition.

[39] G. Catelani, R. J. Schoelkopf, M. H. Devoret, and L. I. Glazman, Relaxation and frequency shifts induced by quasiparticles in superconducting qubits, Physical Review B **84**, 064517 (2011).

[40] J. Koch, V. Manucharyan, M. Devoret, and L. Glazman, Charging effects in the inductively shunted josephson junction, Physical review letters **103**, 217004 (2009).